RECENT ADVANCES IN ULTRAFAST X-RAY ABSORPTION SPECTROSCOPY OF SOLUTIONS

THOMAS J. PENFOLD,[1,2,3] CHRISTOPHER J. MILNE,[1]
and MAJED CHERGUI[1]

[1]*Ecole Polytechnique Fédérale de Lausanne, Laboratoire de Spectroscopie Ultrarapide, ISIC, FSB-BSP, 1015 Lausanne, Switzerland*
[2]*Ecole Polytechnique Fédérale de Lausanne, Laboratoire de Chimie et Biochimie Computationnelles, ISIC, FSB-BSP, 1015 Lausanne, Switzerland*
[3]*SwissFEL, Paul Scherrer Institut, 5232 Villigen, Switzerland*

CONTENTS

Advances in Chemical Physics, Volume 153, Second Edition. Edited by Stuart A. Rice and Aaron R. Dinner.

I. INTRODUCTION

The advent of structural techniques such as X-ray, electron and neutron diffraction, nuclear magnetic resonance (NMR), and X-ray absorption spectroscopy (XAS) has made it possible to directly extract the structure of molecules and condensed matter systems, with a strong impact in physics, chemistry, and biology [1–7]. However, the static structure of the systems under study means that often the mechanisms underlying their function are unknown. Thus, from the early days of femtochemistry, efforts were deployed to implement these structural tools in time-domain experiments [8–11]. Since the first implementation of XAS in a pump–probe type experiment [12] in the micro- to millisecond range, time-resolved XAS has emerged as the method of choice for the study of local structural changes of molecules in solution. The wealth of electronic and geometric information available from an X-ray absorption spectrum has led to its implementation for the study of a wide variety of systems [1–7,13–22].

An X-ray absorption spectrum is characterized by absorption edges, which reflect the excitation of core electrons to the ionization threshold and is consequently element specific. For a particular edge, an electron is initially excited to unoccupied or partially filled orbitals just below the ionization potential (IP) giving rise to bound–bound transitions, which form the pre-edge features. This region, thus, yields information about the nature of the unoccupied valence orbitals, as the transition probability is governed primarily by the atomic dipole selection rules. Above the IP, resonances show up due to interferences of the photoelectron wave from the absorbing atom with the wave scattered back from the neighboring atoms. When the kinetic energy of the electron is large, that is, well above the edge, single scattering (SS) events usually dominate, as the scattering cross section of the photoelectron is small. This region is called the extended X-ray absorption fine structure (EXAFS) region and it delivers information about coordination numbers and the distance of the nearest neighbors to the absorbing atom. In contrast, at low photoelectron energies ($<$50 eV above the edge) contained within the X-ray absorption near-edge structure (XANES) region, resonances arise primarily from the interference of scattering pathways between multiple atoms, that is multiple scattering (MS). This region contains information about the three-dimensional structure around the absorbing atom, i.e. coordination numbers, bond distances, and bond angles.

The methodology for time-resolved XAS has been developed at the beginning of the 2000s [8,9,11,23–30]. It generally consists of an optical pump/X-ray probe experiment operating in a transient absorption geometry, where the laser-induced changes in the sample X-ray absorption coefficient are probed by the X-ray pulse as a function of energy and time delay with respect to the laser pulse. In most cases, the X-ray absorption-induced changes are recorded on a pulse-to-pulse basis with the X-ray transmission through the sample being recorded at twice the repetition rate of the laser [26,31]. In such cases the laser pulse is from an amplified femtosecond system operating at 1 kHz, in order to ensure a high photolysis yield, and the X-ray synchrotron pulses (typically 50–100 ps long) are recorded at a repetition rate of 2 kHz. This implies a significant loss of X-ray flux since synchrotrons operate at MHz repetition rates. In recent years the methodology for time-resolved XAS studies has seen significant developments in both temporal resolution and signal-to-noise ratio (S/N). In particular, the implementation of the slicing scheme [32] has made it possible to demonstrate femtosecond XAS of photoexcited species in solutions [33–36]. In addition, a scheme using a high-repetition rate pump laser, operating at an integer fraction of that of the storage ring [37–39], has allowed exploitation of up to two orders of magnitude more X-ray photons than previous schemes based on the use of kHz lasers for picosecond (ps) XAS experiments. Consequently this has led to over an order of magnitude increase of S/N compared to the previous schemes. Finally, the advent of the X-ray free electron lasers (X-FELs) is opening new opportunities in the area of structural dynamics [40–42], as X-FELs have a 10 orders of magnitude larger flux per pulse, compared to the slicing scheme at comparable temporal resolution.

The complex mechanism behind the origin of X-ray absorption spectra means that their analysis is inextricably linked to detailed theoretical simulations, traditionally performed using MS theory within the limits of the muffin-tin (MT) potential [3]. This approach is computationally very efficient and sufficient when the photoelectron is not sensitive to the details of the potential near the ionization limit. However, the limitation of the MT approximation close to the edge means that such calculations cannot always interpret the entire spectrum, particularly the near-edge region. The above experimental developments as well as continuous improvements in the instrumentation are enhancing the sensitivity of both static and time-resolved XAS experiments, thanks to which finer details of the spectra are uncovered. This calls for more detailed theoretical approaches and the last decade has witnessed significant developments, in particular for the simulation of X-ray absorption spectra beyond the MT potential. These include traditional electronic structure methods extended to core hole excitations [43–45]. In addition, there has been extensive work to move beyond the quasi-particle approximation (QPA), which treats the excited electron as a single particle moving in an average potential. Many-body effects, which arise from the breakdown of this approximation, such as the *intrinsic* and *extrinsic* losses [3], have until

recently been accounted for using a phenomenological broadening of the calculated spectrum [46].

There are already several excellent reviews on both static and time-resolved X-ray absorption spectroscopy [1–3,5–9,11,23,28–30,45]. Therefore, here we focus on the most recent experimental developments and the various state-of-the-art theoretical tools for static and time-resolved XAS of species in solution. This chapter is organized in the following way: In the first section, we recall the basic aspects and recent developments of the XAS methodology. This is followed by a detailed summary of the theoretical approaches for simulating X-ray absorption spectra, before finally presenting some recent highlights.

II. EXPERIMENTAL METHODS

The measurement and analysis of X-ray absorption fine structure (XAFS) data are a significant challenge [2,47] and therefore an effective analysis requires a detailed attention to possible systematic errors. Experimentally this type of spectrum can be realized in several ways, each with its own advantages and disadvantages. In the following sections, the two most commonly used detection methods are discussed, followed by their extension into the time domain.

A. Steady-State XAS

1. Transmission and Fluorescence Detection Modes

The simplest and most common method of measuring the X-ray absorption coefficient is X-ray transmission. Using a tunable monochromatic X-ray beam ($\Delta E/E \sim 0.015\%$) both the transmitted (I_t) and incident (I_0) X-ray signals are measured as a function of incident photon energy [1–3,29,30]. These signals are often measured with ion chambers, where the gas mixture can be varied to maintain detector linearity, or with diodes. The X-ray linear absorption coefficient $\mu(E)$ (in cm^{-1}) is then derived from the Lambert–Beer law:

$$A(E) = \mu(E) \cdot d = \ln\left(\frac{I_\mathrm{t}}{I_0}\right) \tag{1}$$

where d represents the sample thickness. In principle, $\mu(E)$ refers to the total absorption coefficient of the sample, which includes not only the absorber atom but also the environment in which the absorber is contained, along with coherent inelastic Compton scattering.

In contrast, it is sometimes advantageous to measure $\mu(E)$ by monitoring processes that are proportional to the absorption coefficient, such as the X-ray total fluorescence yield (TFY) or the total (Auger) electron signal emitted by the

sample [49]. These are particularly useful when the signal of interest contributes only a small fraction to the total absorption, or when the sample transmission is very large. The fluorescence and Auger signals are due to the absorbing atom only, and in a careful geometrical arrangement, the elastically scattered photons can be discriminated against resulting in a close to background-free measurement. Photon-counting detectors, such as avalanche photodiodes (APD) or photomultiplier tubes (PMT), are often used. If energy-resolving detectors are used (e.g., silicon drift detectors) the elastically scattered photons, which are of higher energy than the fluorescence photons, can be discriminated against improving the sensitivity of the measurement even further.

For fluorescence yield detection, the measured signal, I_f, is proportional to the absorption coefficient $\mu(E)$, but needs to be corrected for the fluorescence quantum efficiency and geometrical factors. As depicted in Fig. 1, the fluorescence yield is proportional to the X-ray intensity I at the point of absorption and the fluorescence efficiency ϵ_A. Therefore, given a measured fluorescence flux at position y, the signal is given by

$$I_\mathrm{f} = I_0 \mu_\mathrm{A}(E) \epsilon_\mathrm{A} \cdot \mathrm{e}^{-\mu(E)y} \cdot \mathrm{e}^{-\mu(E_\mathrm{f})z} \tag{2}$$

where $\mu_\mathrm{A}(E)$ is the absorption coefficient of the absorbing atom, z is the escape depth, $\mu(E)$ is the total absorption coefficient including the environment around the absorbing atom, E is the photon energy of the incident beam, and E_f is the

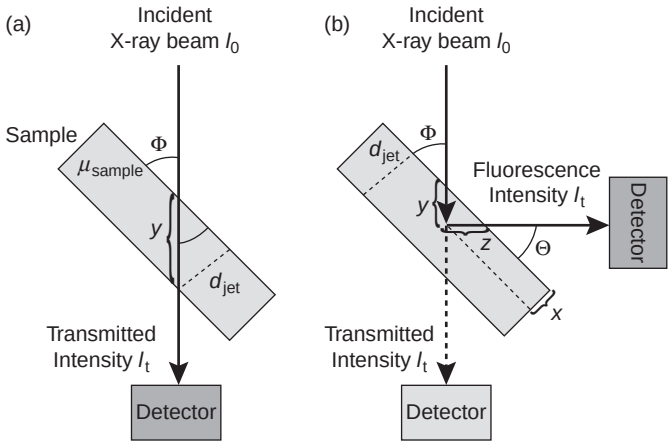

Figure 1. The two most commonly used experimental configurations for measuring XAS are (**a**) transmission and (**b**) fluorescence yield modes. Figure from Ref. [48].

emission energy of the fluoresced photon. After integration over y and z and using the geometry shown in Fig. 1 ($\Phi = \Theta = 45^\circ$) [48], one arrives at

$$I_\mathrm{f} = \frac{I_0 \mu_\mathrm{A}(E) \epsilon_\mathrm{A}}{\mu(E) + \mu(E_\mathrm{f})} \left(1 - \mathrm{e}^{-[\mu(E)+\mu(E_\mathrm{f})]d'}\right) \tag{3}$$

where $d' = d/\sin(45^\circ)$. The fluorescence intensity is thus directly proportional to the absorption coefficient of the absorber, but in addition, the geometrical factors and the quantum efficiency are now included. The above equation can be further approximated in two different experimental limits: the thick-sample [49] and the thin-sample [50] limits. However in both cases, the resulting X-ray fluorescence can be directly related to the changes in the absorption coefficient of the central absorbing atom and thus it should yield quantitatively the same XAS spectrum, as recorded by X-ray transmission [51].

In general X-ray signals are normalized such that the signal well before the absorption edge is set to zero and the post-edge signal is set to 1. This allows more straightforward analysis and comparisons of signals across experiments and to theory. All X-ray signals presented in this chapter are normalized this way.

B. Time-Resolved XAS

1. *General Setup*

Time-resolved XAS experiments are implemented within the laser-pump/X-ray-probe scheme, for which a generalized setup is shown in Fig. 2. Here, an ultrashort laser pulse starts a chemical reaction and a delayed X-ray pulse probes the changes induced in the system by the photoexcitation. The detected transient XAS signals

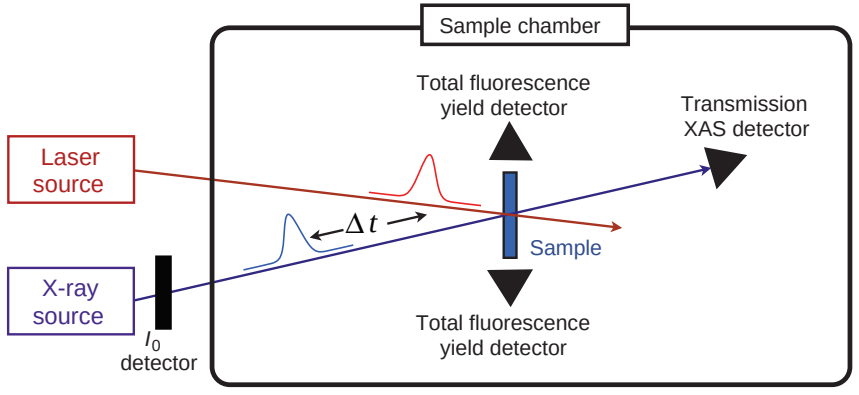

Figure 2. Sketch of the time-resolved XAS setup for the study of liquid samples. The continuously refreshed sample can be a flow capillary, a flow-cell, or a high-speed liquid jet.

will contain all the photoinduced electronic and structural changes between the ground state spectrum and the excited state spectrum. However, the use of an X-ray probe in contrast to an optical probe introduces some specific conditions [8,25,31]. These are as follows:

- An X-ray pulse contains $\sim 10^4 - 10^6$ photons, much less than a typical ultrashort laser pulse that can contain $>10^9$ photons nJ^{-1}. This necessitates an optimization of the sample and the detection system to minimize the number of X-ray photons required to measure a given X-ray absorption cross section with the highest possible accuracy, thus maximizing the S/N [8,28]. The closer the measurement to the shot-noise limit, the more efficiently it can detect small XAS changes.
- *The Absorption Cross Section of X-rays*. Hard X-ray absorption cross sections are typically two to four orders of magnitude smaller than optical cross sections; therefore, the interaction of the sample with the X-ray probe pulse is weak, yielding small X-ray signal changes. Conversely the optical density (OD) of the sample at visible wavelengths is often quite high, resulting in a significant difference between the laser and the X-ray absorption that is far from ideal. Maintaining a balance between the maximum possible X-ray absorption and an optical density that will absorb 90% of the laser photons can be challenging since external factors, like sample solubility, can also affect the conditions.
- To ensure that the X-rays are probing the photoexcited region of the sample they need to be focused to a spot size smaller than that of the laser focus. The laser focus size determines the excitation fluence (mJ cm^{-2}), which is related to the population of the excited state. At typical third-generation bend magnet beamlines, X-ray foci are in the 100–300 μm diameter range. The divergence of the X-ray beam is inherent to the source properties and limits its brilliance. This generally restricts the experiment to a large laser spot size, which requires high pulse energies to maintain sufficient fluence and places limitations on the laser sources used for the experiments. An alternative approach, which is available at some insertion-device (wiggler, undulator) beamlines at third-generation synchrotrons, is to use specialized X-ray optics, for example, Kirkpatrick–Baez focusing mirrors [52–55] or zone plates [56,57], which can significantly reduce the X-ray focal size down to the 1–10 μm range. This allows the use of more diverse laser sources and wavelengths.
- The typical X-ray flux available at a third-generation synchrotron is composed of a train of X-rays pulses (the multibunch, Fig. 3), generally separated by a few nanoseconds (ns). In order to perform pump–probe measurements, an isolated probe pulse must be used. The approach taken by many light sources is to place an isolated electron bunch into the ion-clearing gap of the

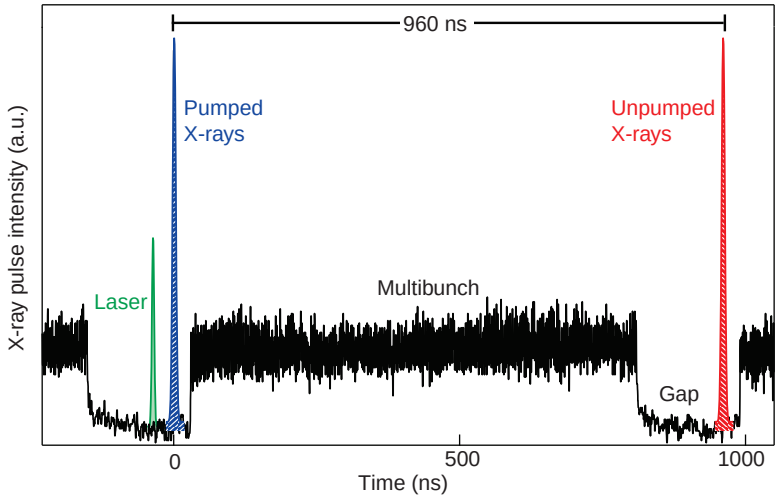

Figure 3. Plot of the X-ray fill pattern at the Swiss Light Source showing the isolated hybrid pulse, the photo excitation laser pulse, the multibunch pulse train, and the ion-clearing gap.

fill pattern (Fig. 3). This gap is typically ∼200 ns long so with fast X-ray detectors, such as APDs or PMTs, it is possible to measure only the X-ray pulse from this isolated bunch (so called *hybrid pulse*), allowing a pump–probe experiment to achieve a time resolution limited by the duration of this X-ray pulse (∼50–100 ps).

Data acquisition of time-resolved XAS signals is based on the measurement of transient absorption spectra, which is the difference between the absorption of the excited sample minus that of the unexcited sample. Briefly, the XAS signal at a specific X-ray energy and pump–probe time delay is recorded at twice the laser repetition rate, alternating between the signal from the excited sample (pumped) and that from the unexcited sample (unpumped). At the Swiss Light Source (SLS) synchrotron (Villigen, Switzerland), the pulse is delivered at a repetition rate of 1.04 MHz. In addition, a zero measurement is made for every X-ray measurement by reading the detector signal in the gap where no X-rays are present. This electronic zero level is then subtracted off the corresponding X-ray signal to compensate for any drifts over time of the data acquisition baseline. The signals provided to the user correspond to the pumped XAS signal ($I_{\mathrm{p}} = [I_{\mathrm{p}}]^{\text{X-ray}} - [I_{\mathrm{p}}]^{\text{zero}}$), the unpumped XAS signal ($I_{\mathrm{unp}} = [I_{\mathrm{unp}}]^{\text{X-ray}} - [I_{\mathrm{unp}}]^{\text{zero}}$) and the pulse-to-pulse difference signal of pumped–unpumped with the zeros being ignored as the electronic baseline will have no time to drift during the interval separating the two X-ray measurements ($I_{\mathrm{diff}} = [I_{\mathrm{p}}]^{\text{X-ray}} - [I_{\mathrm{unp}}]^{\text{X-ray}}$). The reported measurements

can be either simultaneously or separately performed in transmission and/or in fluorescence yield modes. For this dual-mode detection, the results can be averaged to achieve a more efficient data collection and a better S/N; however, this requires a proper definition of the transient spectra recorded in both modes and their comparison, which we will now demonstrate.

2. *Interpretation of the Transient Signal*

The transmitted X-ray intensity can be defined, as in the static case, by the Lambert–Beer law with a slight modification with respect to the photo excitation yield f. If the sample concentration is n_{sam} (in particles mm^{-3}), then the excited state concentration in the laser-excited volume is $f \cdot n_{\text{sam}}$, averaged over the sample thickness d. Given the low X-ray flux available in these experiments, the probing process is linear (this may be reconsidered in the case of X-FELs); therefore, using the Lambert–Beer law, and expressing the transmitted X-ray intensity I_{t} as a function of the fraction of excited state species and the remaining ground state species, $(1 - f) \cdot n_{\text{sam}}$, one obtains

$$I_{\text{t}} = I_0 \cdot \mathrm{e}^{-(1-f)n_{\text{sam}}\sigma_{\text{gr}}d} \cdot \mathrm{e}^{-fn_{\text{sam}}\sigma_{\text{exc}}d} \cdot \mathrm{e}^{-n_{\text{sam}}\sigma_{\text{res}}d} \cdot \mathrm{e}^{-n_{\text{sol}}\sigma_{\text{sol}}d} \tag{4}$$

where n_{sol} and n_{sam} are the solvent and sample concentrations, respectively, σ_{sol} is the X-ray absorption cross section of the solvent molecule, σ_{gr} and σ_{exc} are the X-ray absorption cross sections of the absorbing atom in the ground (unpumped) and excited state (pumped) at a given X-ray energy, respectively. σ_{res} accounts for the X-ray absorption of all residual atoms present in the molecule. Setting $\Delta\sigma_{\text{ex}} = \sigma_{\text{ex}} - \sigma_{\text{gr}}$ and $\sigma_{\text{total}} = \sigma_{\text{gr}} + \sigma_{\text{res}}$, we can rewrite Eq. (4) as follows:

$$I_{\text{t}} = I_0 \cdot \mathrm{e}^{-n_{\text{sam}}\sigma_{\text{total}}d} \cdot \mathrm{e}^{-fn_{\text{sam}}\Delta\sigma_{\text{exc}}d} \cdot \mathrm{e}^{-n_{\text{sol}}\sigma_{\text{sol}}d} \tag{5}$$

Here, the transmitted X-ray intensity is described as a function of the excitation contribution to the signal: $\mathrm{e}^{-fn_{\text{sam}}\Delta\sigma_{\text{exc}}d}$. The transient absorption signal can then be defined as the logarithmic ratio of the unpumped X-ray transmission to the pumped X-ray transmission:

$$\Delta A^{\text{T}}(E,t) = A^{\text{T}}_{\text{p}}(E,t) - A^{\text{T}}_{\text{unp}}(E) = \ln\left(\frac{I^{\text{T}}_{\text{unp}}(E)}{I^{\text{T}}_{\text{p}}(E,t)}\right) = f \cdot n_{\text{sam}} \cdot \Delta\sigma_{\text{exc}} \cdot d \tag{6}$$

where the subscripts p and unp represent the X-ray transmission of the pumped and un pumped sample, respectively. In a similar way, we can define the transient pump–probe signal detected in fluorescence yield mode as

$$\Delta I^{\text{F}}(E,t) = \frac{I^{\text{F}}_{\text{diff}}(E,t)}{I_0(E)} = \epsilon_{\text{A}} \cdot f \cdot n_{\text{sam}} \cdot \Delta\sigma_{\text{exc}} \cdot d = \frac{\Delta A^{\text{T}}(E,t)}{\epsilon_{\text{A}}} \tag{7}$$

This establishes the relation between the transient signals measured in transmission, $\Delta A^{\mathrm{T}}(E,t)$, and fluorescence, $\Delta I^{\mathrm{F}}(E,t)$, modes under the thin-sample limit condition [48]. Both signals are identical apart from the constant factor $1/\epsilon_{\mathrm{A}}$, which accounts for the fluorescence yield probability.

Importantly, this demonstrates that the excitation yield is a critical factor for the accurate characterization of the XAS spectrum of the excited species [28]. It must be precisely known, and since it is rarely measured during the optical pump/X-ray probe experiment, it has to be extracted from a separate optical pump/optical probe measurement under similar conditions. It is important to emphasize that, if the product XAS spectrum is to be accurately extracted, the excitation yield cannot just be estimated from the sample characteristics (optical absorption coefficient, concentration, etc.) and the laser pulse parameters, since this ignores other losses in the sample including scattering and nonlinear absorption contributions.

C. Sources of Ultrafast X-ray Pulses and Data Acquisition

1. Picosecond XAS

As previously noted in Section I, until very recently all time-resolved XAS experiments were performed with the pump laser operating at kHz repetition rates. This means that typically 10^3 of the X-ray pulses are wasted, as synchrotron pulses are delivered at MHz repetition rates. This is a major limiting factor in the achievable S/N of the experiments, which as previously discussed is already a significant challenge. This not only reduces the accuracy of the structural analysis but also places the restriction that samples must have solubilities in the range of tens to hundreds of millimolar (mM) (mmol L^{-1}) and large optical absorption cross sections (OD > 1).

In order to exploit all the available hybrid X-ray pulses, a setup was recently implemented [37] using a ps pump laser having a variable repetition rate that can run at 520 kHz, that is, half the repetition rate of the SLS (1.04 MHz). This represents the most efficient use of all the available isolated pulses, but the laser repetition rate can also be decreased if required due to sample relaxation times (> 1 μs) or if higher laser pulse energies are desired. Provided the conditions (laser fluence, incident X-ray flux per pulse, sample concentration, thickness, etc.) are similar to those of the previous 1 kHz experiments and assuming that the predominant source of noise is the shot noise of the X-ray source, an increase of $\sqrt{520} \approx 23$ in S/N can be expected, resulting in significantly shorter data acquisition times. In fact, an increase of 25–30 was determined in calibration experiments [37]. Similar high-repetition rate pump–probe schemes have in the meantime been implemented at the Advanced Photon Source synchrotron (Argonne, USA) [38] and the Elettra synchrotron (Trieste, Italy) [39]. Better time resolution can be achieved while maintaining the improvements of the high-repetition rate technique by

taking advantage of specialized synchrotron modes such as the *low-alpha* mode [58] or unique ring modifications such as the *crab cavities* [59,60]. Unfortunately both of these techniques will only reduce the pulse duration down to a few ps and this improvement in time resolution comes at a cost in X-ray flux. Subpicosecond resolution is achievable at synchrotrons using the slicing scheme that operates at kHz repetition rates, as discussed next.

2. Femtosecond XAS: The Slicing Scheme

In order to extract fs X-ray pulses from a storage ring, the slicing scheme [32,61,62] was developed, which is based on scattering a femtosecond laser pulse from a relativistic electron bunch within the storage ring [63]. The ultrafast laser pulse copropagates with the electron bunch through a specially designed wiggler and modulates the electron energies of a "slice" of the 50–100 ps long bunch. The slice duration is approximately the temporal width (50–100 fs) of the slicing laser pulse. The electrons are then sent through a chicane that spatially separates them as a function of energy, followed by propagation through an undulator that generates the X-rays. Because the sliced X-rays are spatially separated from the main core beam, it is possible to use spatial filters to isolate the fs X-ray pulses and use them for measurements. The resulting pulse duration at the SLS slicing source is 170 fs [62]. The drawback of this scheme is the drastically reduced X-ray flux, which is typically a thousandth that of a typical synchrotron pulse. This decrease in flux makes XAS experiments quite challenging, due to the requirements for energy resolution ($<$2 eV) but for ultrafast X-ray diffraction, the slicing scheme has proven very successful [64–73], as a high energy resolution is not required. The slicing scheme at the SLS was first applied to XAS at the Fe K-edge ($\sim$7 keV) for the study of Fe(II)-based complexes in solution undergoing a light-induced ultrafast spin crossover [33]. It has also been extended to the soft X-ray regime by Huse et al. [36] in their study of the same process at the Fe L edges (700 eV).

3. Future Developments: X-FELs

The advent of the X-FELs offers new and exciting opportunities for structural dynamics in solution chemistry and biochemistry [41,74,75]. These sources deliver coherent X-rays in the wavelength range 0.1–10 nm and temporal width of 10–100 fs, with a peak brightness over 10^{10} times that of a third-generation synchrotron. In particular for XAS, X-FELs make it possible, in principle, to follow chemical dynamics of molecules in solution on ultrafast timescales, with very high S/N. However, restrictions due to photon energy tunability and the stability of the spectral and temporal characteristics of the source still need to be improved to make them usable for such studies. Indeed, the FEL photon energy can fluctuate outside its own bandwidth from shot to shot, resulting in $\sim$100% intensity fluctuations

after the monochromator [76]. In addition, timing jitter between the excitation laser and the X-FEL has limited the temporal resolution thus far to ∼300 fs, though recent improvements make it possible to rebin data using a shot-to-shot cross-correlator, resulting in 120 fs time resolution [77]. Therefore, at present, synchrotrons remain the most reliable source of X-ray photons for time-resolved XAS, although this situation may change in the near future. Combined with the slicing scheme or an ultrafast X-ray streak camera [78–81], they will continue to provide the subpicosecond to picosecond time resolution. It is also important to note that although the per-pulse X-ray flux is much higher at X-FELs, the average flux per second is comparable, or even lower than at undulator-based synchrotron beamlines (10^{12} photons s^{-1}).

The first femtosecond X-ray absorption spectra obtained using an XFEL have recently been published [82].

III. THEORETICAL APPROACHES FOR XAFS

As for all spectroscopies, the starting point for calculating an X-ray absorption spectrum is the Fermi Golden Rule (FGR)

$$\mu(E) \propto 2\pi \sum_f |\langle \Psi_f | \hat{H}_{\text{int}} | \Psi_i \rangle|^2 \delta(E_{\text{if}} - \hbar\omega) \tag{8}$$

It describes the transition from an initial state (Ψ_i) to a final state (Ψ_f), where in both cases Ψ represents the full many particle wavefunction. $\hat{H}_{\text{int}}$ is the interaction Hamiltonian, typically within the dipole or dipole + quadrupole approximation.

In contrast to simulating valence level spectroscopy, the necessity to accurately describe both the localized core electrons and the diffuse continuum states presents a significant computational challenge. In addition, many-body effects are often important, but their inclusion is far from trivial. The development of MS approaches [3,83,84] revolutionized this domain, making it possible to simulate the whole spectrum in a computationally efficient manner. So far, most of these implementations have been within the limits of the MT approach, which approximates the potential as nonoverlapping spherical cells centered at each atomic site. For EXAFS spectra this gives a good agreement with experiment because at energies well above the edge, the photoelectron is not sensitive to the finer details of the potential near the IP. However, and in particular with the improvement in the quality of experimental data, the MT approximation is often no longer sufficient to describe the fine details of the XANES spectrum. This is vital for understanding time-resolved experimental signals because the largest changes occur in the XANES region of the spectrum. These limitations have led to an intense effort in theoretical developments culminating in dramatic progress over the past decade. In the following section, we give a description of the theoretical approaches for simulating X-ray absorption spectra, detailing the current status and recent progress.

A. Structural Analysis: The EXAFS Region[1]

Extracting the fine structure oscillations associated with the EXAFS spectrum is a critical step and a thorough understanding of the theory is a prerequisite for a meaningful analysis. However, it is not our intention to present this here, and instead, we refer the reader to previous reviews [6,85] and commonly used methods [86,87].

Once extracted, the EXAFS spectrum can be routinely simulated using the EXAFS equation [2,3,83]

$$\chi(k) = \sum_{\gamma} \frac{N_\gamma S_0^2 |f_{\text{eff}}(k)|}{kR_\gamma^2} e^{-2R_\gamma/\lambda_{\text{tot}}(k)} e^{-2\sigma^2 k^2} \sin(2kR_\gamma + \phi_\gamma) \qquad (9)$$

Here, γ is the scattering path index with degeneracy N_γ. The half-path distance and the squared Debye–Waller (DW) factor are represented by R_γ and σ^2, respectively. In addition, $f_{\text{eff}}(k) = |f(k)| \exp^{i\phi(k)}$ is the complex backscattering amplitude for path γ, ϕ_γ is the central atom phase shift of the final state, and $\lambda_{\text{tot}}(k)$ is the energy-dependent mean free path. S_0^2 is the overall amplitude reduction factor that accounts for many-body effects (see Section III.C).

This equation comprises two components, amplitude (the first three terms) and phase (the final, *sine* term). The amplitude contains information about the nearest neighbors (coordination), atomic species and disorder, while the phase component consists of interatomic distance and a phase factor that has a k dependence arising from an increase in the kinetic energy close to the atomic core [85]. Unfortunately, both the amplitude and the phase depend only very weakly on the atomic species and this means that it can be difficult to identify an unknown scatterer with precision from an EXAFS analysis. For most chemical complexes this is not a problem because their composition is known. However for larger systems of biological interest this can be important, as was recently demonstrated for the nitrogenase iron–molybdenum cofactor [88].

The resolution can be enhanced by scaling the spectrum in k-space with different weighings (typically k, k^2, or, k^3), but this does not generally help distinguish very similar atoms, for example, C, O, N, and S. Funke et al. [89] and Munoz et al. [90] have recently presented approaches based on a wavelet transform. This yields a 2D correlation plot in both R- and k-space (analogous to a time–frequency correlation plot). This can help distinguish atomic species, especially for atoms at a similar distance from the absorber. Interestingly, the properties of wavelets are making them increasingly attractive for molecular systems [91] and a method for calculating the XANES spectrum within this basis has been implemented in the BIGDFT [92] package. However, at present, we are unaware of any applications.

Following extraction of the EXAFS fine structure oscillations, the structural information is usually refined using a fit of the spectrum, for which there are

[1] The implementation of the wavelet transform has recently been done [93].

numerous packages available [94–97]. Initially an EXAFS calculation is performed to extract the details of the scattering paths. From these the most important are selected and, in addition to variables including the amplitude reduction factor, the Debye–Waller factor, and the phase shift, they form the parameter space to be optimized.[2] This is routinely performed for the EXAFS spectrum, but has recently been extended for fitting the XANES spectrum [99–101]. This represents a more challenging problem, in particular, for obtaining an accurate description of both the spectral convolution (used to account for many-body effects) and the potential. Most notably, the MXAN method [99] has been applied with success to fit a wide variety of problems, including the heme protein myoglobin [17–19].

B. The Quasiparticle Approximation: Modeling the Near Edge

Simulations for the EXAFS spectrum are routinely performed and, because the photoelectron is largely insensitive to the details and response of the potential, agreement with the experimental spectra is generally good. The picture is somewhat different for the XANES spectrum for which the agreement is often qualitative rather than quantitative. Solving the FGR using the full many-body wavefunction, as described in Eq. (8), is obviously not possible and therefore the first approximation made is the so-called quasi-particle approximation (QPA). This assumes that the excited electron propagates through a molecule, behaving as a quasiparticle moving in an effective potential and, the Hamiltonian comprises the single particle terms plus a self-energy operator (see Section III.C.1). A physical illustration of this approximation is that the XANES spectrum for K-edges can often be approximated (within the dipole approximation) from the p density of states (DOS) of the absorbing atom. This is because for these spectra the many-body effects tend to be small. The simplifications brought about by the QPA has led to it becoming the cornerstone of XANES calculations, making the FGR for such spectra a tractable problem. In this section, we outline the most commonly used approaches for simulating XANES spectra.

1. Green's Functions and Multiple Scattering Theory

In simulating X-ray absorption spectra, even within the QPA, the major limitation is the requirement to calculate the final states. The most commonly adopted approach is that of multiple scattering theory [3,83,102,103]. Here, instead of explicitly calculating the final states, the FGR is expressed in terms of the photoelectron Green functions, that is, of the ground state matrix elements. The power of this approach lies in its ability to separate the final state into scattering sequences, each sequence involving individual potential cells with free-particle propagation

[2] In such procedures it is important to comply with the Nyquist criterion [98], describing the minimum ratio of independent points compared to the number of fitting variables for a meaningful fit.

between the events. This gives rise to the picture of multiple scattering of the free photoelectron from sequential atomic sites, and therefore the resonances are often described in this manner. However, it should be emphasized that this approach is valid both below and above the IP and the scattering order represents the extent to which the final state is distorted from the atomic symmetry of the absorber.

Within multiple scattering theory, the FGR [Eq. (8)] is rewritten in the form of a sum of Green's functions:

$$\mu(E) \propto -\frac{1}{\pi}\Im \sum_i |\langle i|\epsilon \cdot \mathbf{r} G(\mathbf{r}, \mathbf{r}'; E)\epsilon \cdot \mathbf{r}'|i\rangle|^2 \delta(E_{\text{if}} - \hbar\omega) \tag{10}$$

The propagator $G(\mathbf{r}, \mathbf{r}', E)$ can be expressed as contributions of the absorbing atom (G^{c}) and the surrounding atoms (G^{sc}):

$$G(\mathbf{r}, \mathbf{r}'; E) = G^{\text{c}}(\mathbf{r}, \mathbf{r}'; E) + G^{\text{sc}}(\mathbf{r}, \mathbf{r}'; E) \tag{11a}$$

$$G^{\text{sc}}(E) = \bar{G}T\bar{G} + \bar{G}T\bar{G}T\bar{G} + \cdots \tag{11b}$$

$$G^{\text{sc}} = (1 - \bar{G}T)^{-1}\bar{G} \tag{11c}$$

G^{sc} is then solved either as a sum over all MS paths [Eq. (11b)] or as a matrix inversion, that is, full MS [Eq. (11c)]. $\bar{G}$ represents the free Green's function damped by the complex self-energy operator (see Section III.C.1). The separation of the propagator into individual scattering sites imposes that these calculations are carried out at nonoverlapping potential cells; however, as demonstrated by Williams and Morgan [104] there is no limitation on this shape, except the fact that they are nonoverlapping. Difficulties in formulating a useable approach based upon nonoverlapping potential cells means that such calculations have been so far limited to the MT potentials. Recently, the spectra have been improved by using overlapping MT [105]. When the overlap is around 10–15% the benefit can remain greater than the error; however, this approach is mathematically incorrect and these false improvements can hide structural or electronic information [106]. Importantly there have been attempts to extend traditional MS theory beyond the MT potential. Most notably, a recent paper by Hatada et al. [84] presented a method for full potential MS based upon space filling cells [107].

Despite the aforementioned limitations, multiple scattering theory provides, for many cases, a satisfactory description of the X-ray absorption spectrum and should always be the first calculation performed. Due to its wide application, there has been considerable work aimed at overcoming the limitations and reducing its computational expense, which are discussed in detail in Ref. [108].

2. *Beyond Spherical Potentials*

At present, for systems that are poorly described within the limits of the MT approximation, the most widely used alternative is the finite difference method (FDM) near-edge structure (FDMNES) approach by Joly [106,109]. For these calculations, the system is decomposed into three regions, (i) the atomic core, (ii) the continuum, and (iii) the valence region. The FDM is used to solve the wavefunction in the important valence region, while the continuum (which has a constant potential) is solved using a basis of Neumann and Bessel functions. The atomic core is described using spherical harmonics, similar to the approach of the MT potential. But in this case the spherical region is smaller than that typically used in the MT approach. In fact it is only used to save the computational expense associated with having the dense grid required to accurately describe the potential close to the nucleus.

In solving the wavefunction in the FDM region the Schrödinger equation is expressed as

$$(-l_{ii} + V_i - E)\psi_i + \sum_{j}^{\text{neighbors}} -l_{ij}\psi_j = 0 \tag{12}$$

Here l_{ii} is the Laplacian operator, composed of an approximation of the wavefunction around the grid point i using a fourth-order polynomial. In solving this equation, particular care has to be taken to ensure a continuous behavior of the wavefunction across the boundaries of the three regions.

This approach offers significant improvements to the MT potential, and its applicability has been demonstrated on numerous molecular systems [110–113]. However, the major limitation is that these calculations are computationally expensive. This comes from the maximum angular momentum used to connect the interstitial region to the outer sphere, given by

$$kr = \sqrt{l_{\max}(l_{\max+1})} \tag{13}$$

where k is the photoelectron wave vector and r is the cluster radius. In the absence of symmetry, this limits its application to clusters of not more than 30 atoms [114].

Other approaches beyond the limitation of nonoverlapping potential cells have been implemented using plane waves. The ability of plane waves to describe the diffuse continuum states is well established [115–118]; however, pseudopotentials have to be used for the core levels, meaning that these approaches often lack physical transparency. Hütter and coworkers have extended their Gaussian augmented with plane waves method [119,120] to core hole spectra [121,122]. This approach benefits from describing the continuum states in a plane wave basis, while still explicitly calculating the core states in an efficient manner within the Gaussian basis. It has been used to calculate the spectra for bulk water and small organic

complexes [123,124], and although promising, its applicability still needs to be demonstrated on a large variety of systems.

C. Many-Body Effects

Despite the effectiveness of the QPA there are some significant failures that have to be addressed in order to obtain an accurate description of the spectrum. These arise from correlations between electrons, giving rise to many-body effects. These are most commonly associated with the discrepancies between experiment and theory for the $L_{2,3}$ edge spectra, which are reflected by deviations from the statistical (2:1) branching ratio [125,126] and have been traditionally simulated using multiplet theory [5,7,127].

In addition to multiplets, many-body effects are the origin of inelastic losses (giving rise to the mean free path) [128], plasmon excitations, shake-up and shake-down transitions [129], and the atomic X-ray absorption fine structure (AXAFS) effect, which is due to the scattering of the photoelectron at the periphery of the absorbing atom [130–132]. Since the scattering process is determined by the binding energies of the electrons in the various orbitals, the AXAFS is likely to change between the ground and excited state species in a time-resolved experiment.

These many-body effects are commonly subdivided into two groups, namely *extrinsic* and *intrinsic* losses [3]. The former arise from the dynamically screened exchange interaction between the photoelectron and the system, and they give rise to physical variables such as the mean free path. In contrast, the latter denote many-body excitations that are analogous to a higher order excitation expansion space in configuration interaction (CI). At present, these effects are usually accounted for in a phenomenological manner. At high enough energies, above the edge, the sudden approximation is valid because the excited electron is no longer sensitive to the fine details and response of the potential to the creation of a core hole. In this case, the many-body effects can be estimated as the overlap between the $N-1$ electrons not involved in the excitation:

$$S_0^2 = |\langle \Psi_0'^{N-1} | \Psi_0^{N-1} \rangle|^2 \tag{14}$$

S_0^2 is the amplitude reduction factor, as seen in the EXAFS equation and it usually has a value between 0.8 and 1. Closer to the edge, one typically uses a Lorentzian broadening function to describe the core hole lifetime and an energy-dependent component to account for the inelastic losses [17,46,133]. These components have a clear physical meaning and are not adjustable parameters. Despite its physical basis this approach does not include the fact that *extrinsic* and *intrinsic* losses are quantum mechanically indistinguishable and therefore interference effects close to the edge will be important [134]. It is, therefore, desirable to be able to describe

them in an *ab initio* manner, and recent progress in this respect are presented hereafter.

1. The Self-Energy Operator

The most routinely used approach for including many-body effects is through the self-energy operator (Σ), analogous to the exchange-correlation potential $V_{xc}(\rho)$ of density functional theory (DFT). This energy-dependent complex variable describes the inelastic losses and is added to the Coulomb potential in the single-particle Hamiltonian [135],

$$h' = \frac{p^2}{2} + V_{\text{Coul}} + \Sigma(E) \tag{15}$$

It consists of a real part accounting for the energy dependence of the exchange and an imaginary part that yields the mean free path:

$$\lambda \sim \frac{k}{\Im[\Sigma(E)]} \tag{16}$$

In practice the Hedin–Lundqvist self-energy, $\Sigma_{\text{HL}}(E, \rho)$ [136,137], based on the uniform electron–gas model, is most commonly used. This is written as

$$\Sigma(\boldsymbol{r}, \boldsymbol{r}', E) = \Im \int \frac{\mathrm{d}\omega}{2\pi} G(\boldsymbol{r}, \boldsymbol{r}', E - \omega) W(\boldsymbol{r}, \boldsymbol{r}', \omega) \tag{17}$$

for which the dynamically screened Coulomb potential matrix is $W = \epsilon^{-1} v$, where ϵ^{-1} is the inverse dielectric matrix and v is the bare Coulomb potential. If W is replaced by v, then Σ in Eq. (17) becomes the Hartree–Fock (HF) self-energy. The dielectric matrix is typically calculated within the single plasmon pole approximation of Hedin and Lunqvist [136–138]; however, close to the edge the energy loss spectrum ($\Im[\epsilon(\omega)^{-1}]$) is often broad and relatively structured and therefore it is not well represented within this single pole approximation. To overcome this limitation Rehr and coworkers have recently implemented a many-pole approach, which is modeled to an *ab initio* dielectric constant over a selected spectral range. The energy loss spectrum is then represented as a linear combination of these poles in the form [128]

$$-\Im[\epsilon^{-1}(\boldsymbol{q}, \omega)] = \frac{\pi}{2} \sum_j g_j \omega_j \delta(\omega - \omega_j)(\boldsymbol{q}) \tag{18}$$

where $g_j = (2\Delta\omega_j / \pi\omega_j)\Im[\epsilon(\omega_j)^{-1}]$ is the strength of pole j; $\Delta\omega_j$ is the pole spacing.

In addition to inelastic losses this model has been used, in conjunction with the quasiboson model of Rehr and coworkers [134], to calculate the satellites and other many-body excitations [134,139]. For this the *quasiparticle* spectrum is convoluted

with an energy-dependent spectral function, composed of *extrinsic*, *intrinsic*, and interference terms that are calculated from the many pole loss function [128,134].

2. *Time-Dependent Density Functional Theory*

Using the QPA, an X-ray absorption spectrum is simulated within the initial (ground state configuration) or final (density in the presence of a core hole) state rules [3]. To go beyond this, the cross section can be written as an interacting response function, χ [140] and therefore include the relaxation effects of the system following the creation of a core hole. This can be solved using the Bethe–Salpeter equation (BSE), which includes two-particle excitations (excitons), but is usually computationally expensive [141]. Alternatively one can work within the framework of time-dependent density functional theory (TD-DFT) [142–144]. Here, the density response can be expressed in a Dyson form as

$$\chi = \chi_0 + \chi_0 (v + f_{\mathrm{xc}})\, \chi \tag{19}$$

where χ_0 is the polarizability of the noninteracting (unperturbed) system. f_{xc} is the exchange-correlation functional, which, within the adiabatic approximation (i.e., the time dependence is neglected and therefore the system has no memory effects), is defined as $\delta^2 E_{\mathrm{xc}}[\rho]/\delta\rho(\boldsymbol{r})\delta\rho(\boldsymbol{r}')$. Alternatively setting $f_{\mathrm{xc}} \to 0$, Eq. (19) becomes the time-dependent HF response, commonly referred to as the random-phase approximation (RPA).

In the last decade, TD-DFT has become one of the most widely used methods in quantum chemistry and is now routinely used to study the valence excitations of molecules. In such cases, the density response of linear response time-dependent density functional theory (LR-TD-DFT) is more commonly written in the form of Casida's matrix equation [144,145]:

$$\begin{pmatrix} \mathbf{A} & \mathbf{B} \\ \mathbf{B} & \mathbf{A} \end{pmatrix} \begin{pmatrix} \mathbf{X} \\ \mathbf{Y} \end{pmatrix} = \omega \begin{pmatrix} \mathbf{1} & \mathbf{0} \\ \mathbf{0} & -\mathbf{1} \end{pmatrix} \begin{pmatrix} \mathbf{X} \\ \mathbf{Y} \end{pmatrix}, \tag{20}$$

where $\mathbf{X}$ and $\mathbf{Y}$ represent excitation and deexcitation operators, respectively[3] and the matrix elements $\mathrm{A}_{ia,\,jb}$ and $\mathrm{B}_{ia,\,jb}$ are written:

$$A_{ia,\,jb} = (\epsilon_a - \epsilon_i)\delta_{ai,\,jb} + (ia|\, f_{\mathrm{xc}}|\, jb) \tag{21a}$$

$$B_{ia,\,jb} = (ia|\, f_{\mathrm{xc}}|\, jb). \tag{21b}$$

[3] Equation (20) is often solved by neglecting the Y component. This is called the Tamm–Dancoff approximation (TDA) [146]. The energetics within the TDA are usually indistinguishable from the full treatment, and decoupling the excitations from the deexcitations simplifies the working equations. However, within this approximation, the Thomas–Reiche–Kuhn f-sum rule ($N = \sum_i f_i$, N is the number of electrons) is not conserved, and therefore care should be taken when using the oscillator strengths obtained.

The labels i, j refer to occupied spin orbitals and a and b refer to unoccupied spin orbitals. The solution of Eq. (20) yields the transition frequencies ω and transition amplitudes X_{ia}, Y_{ia}, which are used to calculate the dipole and quadrupole moments [15].

Recently significant work has been deployed in extending this approach to core hole spectra. Converting this expression from valence excitations to core excitations is achieved by a projection onto a manifold of single core to valence excitations [43–45]. This neglects the coupling to other excitations, however the large energy separation that exists between the K-edge (transitions from the 1s orbitals) and the other excitations makes this approximation reliable [15]. As a result, these calculations yield transitions that give at least a qualitative, and often quantitative, description of the preedge region of the spectrum under study. However, the absolute transition energies are typically shifted by 50–300 eV compared to the experiment. This is primarily due to the use of the *sudden approximation*, which neglects electronic relaxation upon ejection of the core electron. In order to characterize the effect of this approximation, Ray et al. [147] performed a detailed calibration of these errors and showed that for a particular atomic edge, the energy shift is almost independent of the surrounding ligands within the limit of the same calculation variables (i.e., basis set, functional etc.).

Although such calculation are not limited to the preedge region, most implementations use a localized Gaussian basis set, which are unable to describe the diffuse continuum states. In addition, they are also subject to the same deficiencies as valence excitations within TD-DFT, namely the well-documented charge-transfer (CT) problem [148]. To illustrate this, Fig. 4 shows the simulated K-edge spectra of [Mn(II)(terpy)Cl_2] with a varying amount of HF exchange [149], which reduces the charge-transfer problem due to its nonlocal nature. Here, the intensity and position of the 1s$\rightarrow$3d and metal-to-liquid charge transfer (MLCT) transitions change dramatically upon increasing the percentage of HF exchange, a classic symptom of the charge-transfer problem.

In the case of heavier elements, relativistic effects are important [150]. For K-edges, the spin-orbit coupling (SOC) constant of the 1s levels is zero, meaning that only scalar relativistic effects need to be accounted for. This can be efficiently achieved using, for example, the zero-order relativistic approximation (ZORA) [151,152]. However for L-edges this is no longer possible due to the strong SOC of the 2p orbitals. The standard formulation of TD-DFT, within the adiabatic approximation [144] is based upon pure density functionals, and therefore it can only yield one of the triplet states, namely the transition that maintains the spin quantum number, M_s. Fronzoni et al. [153] have extended the noncollinear (spin-flip) TD-DFT scheme of Wang et al. [154,155] for core hole excitations, which they applied to calculate the preedge $L_{2/3}$-edge spectra of the $TiCl_4$ complex. They obtained good agreement with the experimental spectra; however, this is a

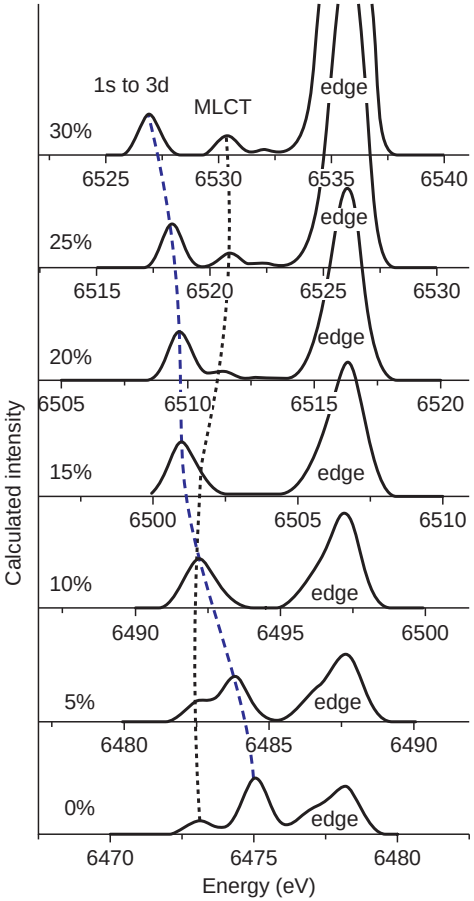

Figure 4. Calculated spectra of $[Mn(II)(terpy)Cl_2]$ with a series of functionals with a varying amount of HF exchange. Starting with no HF exchange, the percentage increases in steps of 5% up to a maximum of 30%. It is seen that the position of the MLCT peak (black dotted line) relative to the 1s→3d peak (blue dashed line) changes from lower in energy (0%, 5%) to the same energy (10%, 15%) to higher energy (20% and higher) depending on the percentage of HF exchange. Reprinted with permission from Ref. [149].

d^0 complex and although it can be applied to closed shell systems of this nature, it cannot accurately describe the excitations for open shell and partly filled d-orbitals, for which the multiplet effect is much larger, and single reference approaches such as TD-DFT are no longer sufficient.

The above application of TD-DFT is focused on characterization of the preedge transitions. However, as asserted earlier, this approach is not limited to this region of the spectrum and can be used above the edge to go beyond the QPA. In particular, Rehr and coworkers [156] have recently implemented a mixed model based upon a local Kernel, employing TD-DFT within the adiabatic local density approximation (ALDA) exchange-correlation functional ($f_{xc} = (\boldsymbol{r} - \boldsymbol{r}')\delta^2 E_{xc}[\rho]/\delta\rho$) and the

nonlocal part treated within the BSE. Here, the response Kernel is partitioned in the forms:

$$K^{\mathrm{L}}(\boldsymbol{r}, \boldsymbol{r}', \omega) = v(r, r') + f_{\mathrm{xc}}(r, r', \omega) \tag{22a}$$

$$K^{\mathrm{NL}}(\boldsymbol{r}, \boldsymbol{r}', \omega) = W(\boldsymbol{r}', \boldsymbol{r}, \omega) - f_{\mathrm{xc}}(\boldsymbol{r}, \boldsymbol{r}', \omega) \tag{22b}$$

The local, K^{L}, can be recognized as the TD-DFT kernel [Eq. (19)]. The results obtained using this approach, referred to as the projection operator method Bethe–Salpeter equations (PMBSE), are formally equivalent to the BSE, but it becomes increasingly difficult to implement as the photoelectron energy increases. To reduce the computational expense one can treat only the local components, using the time-dependent local density approximation (TDLDA) [156].

It is worth noting that, although it is generally considered that the nonlocal and frequency-dependent components of the BSE are required to treat two particle excitonic effects, recent work [157,158] has demonstrated that such effects can be incorporated within specific forms of $\mathrm{f_{xc}}$, providing a very computationally efficient way of obtaining the response. However, to our knowledge these have not yet been applied to XAS.

3. Post-Hartree–Fock Methods

Finally, in a similar vein to TD-DFT adapted for core hole excitations, there has been a significant amount of work extending post-HF methods into this domain. Such methods, as is well known from standard valence excitations, describe the excited state wavefunction as orders of excitation operators, giving a better description of multiplet effects. Nooijen et al. [159] and Coriani et al. [160] have developed approaches based upon the coupled cluster theory. These provide a very accurate description of the initial and final state wavefunctions, they are however presently limited to small molecules.

Alternatively Asmuruf and Besley have proposed a method based upon configuration interaction singles with perturbative doubles correction (CIS(D)) [161], which is a second-order perturbative correction to single excitation configuration interaction (CIS) [162]. For valence excited states, CIS(D) often provides a similar accuracy to TD-DFT; however, because it includes exact HF exchange one could anticipate some improvements in comparison to TD-DFT, particularly when nonlocality is important. In addition, its efficiency means that like TD-DFT it can be applied to larger systems. Following its implementation, it has been applied to study the near-edge spectra of several small organic complexes giving a good description of the spectra and a mean error in the absolute peak positions of $\sim$1–3 eV [161].

In a similar vein, Neese et al. [164] have recently proposed the restricted open-shell configuration interaction singles (ROCIS) method. Their approach expands

a reference HF wavefunction with five excitation classes [164]; in addition, spin flip excitations are included through quasidegenerate perturbation theory using the one-electron SOC operator [168]. However, the limitation of applying excitations to a HF reference is that in many cases, especially for transition metals, the lack of correlation makes it an inadequate starting wavefunction. To overcome this limitation, Neese et al. have incorporated restricted open-shell Kohn–Sham orbitals into the CI matrix, for which the parameters of the mixing have been obtained from a fit to a test set of molecules. The effectiveness of the ROCIS method is demonstrated in Fig. 5 that shows the calculated $L_{2,3}$-edges for $[Fe(bpy)_3]^{2+}$ in solution and compares it to the experimental spectrum [163]. Importantly, the branching ratio and energy gap between the $L_{2,3}$-edges are correctly described. In addition, all of the major features are reproduced, except one ($\sim$712 eV), which is slightly shifted compared to the experimental spectrum.

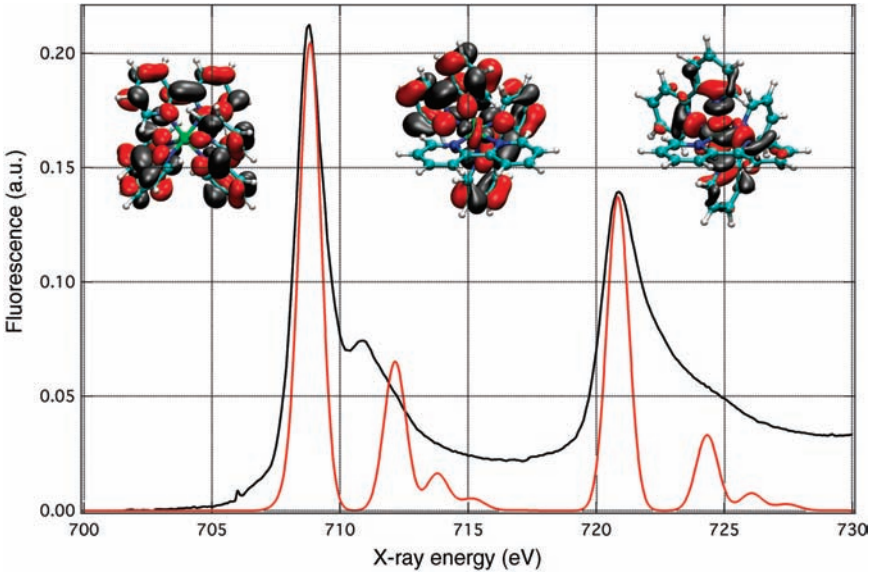

Figure 5. Experimental (black) and calculated (red) $L_{2,3}$-edge spectra of $[Fe(bpy)_3]^{2+}$ in acetonitrile. The experimental spectrum was recorded in total fluorescence yield mode [163]. Insets are molecular orbitals, which are important for the main resonances. The simulations were performed using the restricted open-shell configurational interaction singles (ROCIS) method implemented within the ORCA package [164,165]. A CP(PPP) basis set [166] was used for the iron, while the remaining atoms were described using a TZVP basis. The calculation used a dense integration grid (ORCA Grid4) and the B3LYP functional [124,167] was used for the incorporation of Kohn–Sham orbitals into the CI matrix. The simulated oscillator strength have been broadened with a Lorentzian function to account for core hole lifetime effect.

D. Beyond Picosecond Temporal Resolution

In the previous sections, we have outlined the theoretical approaches necessary to accurately simulate X-ray absorption spectra. For most present applications, the temporal resolution of third-generation synchrotrons means that the data obtained are *quasistatic*. Therefore, the dynamical effects can often be neglected in the simulations. Subpicosecond X-ray absorption spectra, which can presently be achieved using the slicing scheme [33,35], and which will be increasingly available with the X-FEL sources, means that this picture will no longer be valid.

An X-ray absorption experiment with femtosecond resolution will make it possible to map out the reaction path for the system under study. To simulate it one will require efficient computational tools, which explicitly include the effect of the surrounding environment and its response to a perturbation. Such simulations can be performed using molecular dynamics (MD) within the quantum mechanics/molecular mechanics (QM/MM) framework [169–174]. Here, the system is partitioned into a quantum and a classical part that enables the explicit inclusion of solvent molecules in an accurate and computationally efficient manner. This approach was recently extended by Rothlisberger et al. [175] to include nonadiabatic effects using Tully's trajectory surface hopping methodology [176] with all of the relevant quantities, namely electronic energies, nuclear forces, nonadiabatic coupling vectors, and transition dipole elements calculated on-the-fly within LR-TDDFT [177,178].

A complication in such cases is that for systems for which there are several competing pathways, and/or are heavily influenced by the surrounding solvent environment, a number of trajectories are required to obtain a statistically realistic description and replicate the ensemble averaged signal from the experiment. Although possible, this obviously has a significant computational expense associated with it. An example of such a simulation for the analysis of subpicosecond XAS transients of photoexcited aqueous iodide is given below.

IV. EXAMPLES

Several examples of time-resolved XAS studies of atomic and molecular systems in solution have been presented in recent reviews [8,9,11,23,27–30]. Rather here, we will present a few recent experimental examples to illustrate how they are interpreted using the more recent theoretical developments described above. We will also point to ongoing problems of the theory in interpreting XAS spectra.

A. Photoinduced Hydrophobicity

The properties of solvated atomic species and the role of the surrounding water molecules are important in a large variety of chemical and biochemical

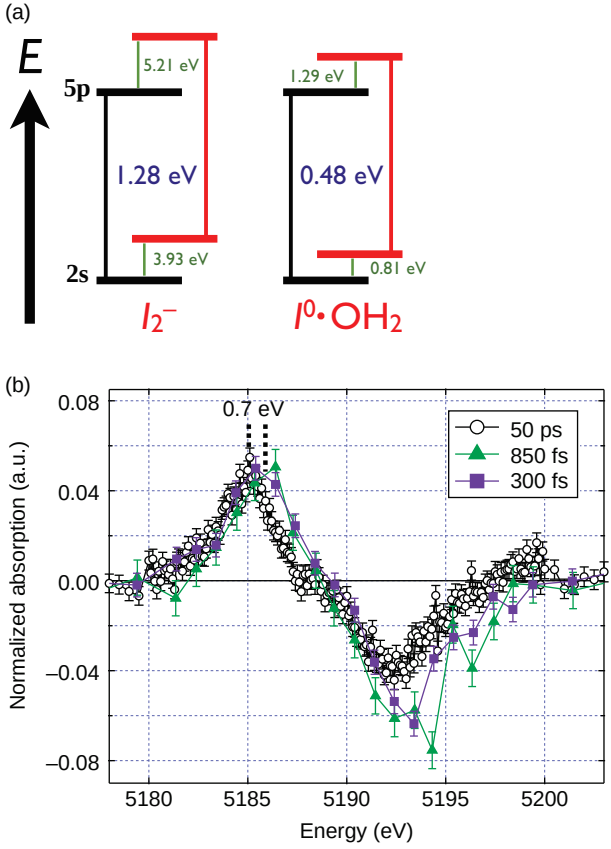

Figure 6. (**a**) Calculated energy shifts with respect to the bare iodine atom of the 2s and the 5p orbitals (in green color) upon formation of diiodide and of the I^0–OH_2 complex obtained at CCSD level of theory. The energy values in blue represent the calculated shifts of the 2s→5p transition. (**b**) Normalized transient L_1-edge spectra of photoexcited aqueous iodide at 50 ps (black markers), 300 fs (green markers), and 850 fs (purple markers) time delays after excitation. The subpicosecond transients were multiplied by a factor of 1.75 in order to match the value of the 50 ps transient at the maximum of the positive feature. Reproduced from Ref. [35].

processes [179,180]. Of particular importance to these is the nature of hydrophobic and hydrophilic solvation, which are considered the main driving forces. Recently, we have used picosecond and subpicosecond XAS to characterize the changes observed upon photoinduced electron abstraction from aqueous iodide, which reflect the transition from hydrophilic to hydrophobic solvation [35,181,182].

Figure 6b shows the comparison between the transient XAS measured at the iodine L_1-edge at various time delays after multiphoton excitation at 400 nm. Laser ejection of an electron from iodide, creating iodine, opens a hole in the 5p valence shell. This makes possible an electronic transition from the 2s core state to the 5p orbital that appears as a preedge absorption around 5185 eV of the L_1-edge. Importantly, Fig. 6 shows clear differences between the subpicosecond timescale and the 50 ps measurement, with the 2s-5p resonance being broadened on its blue side at short times.

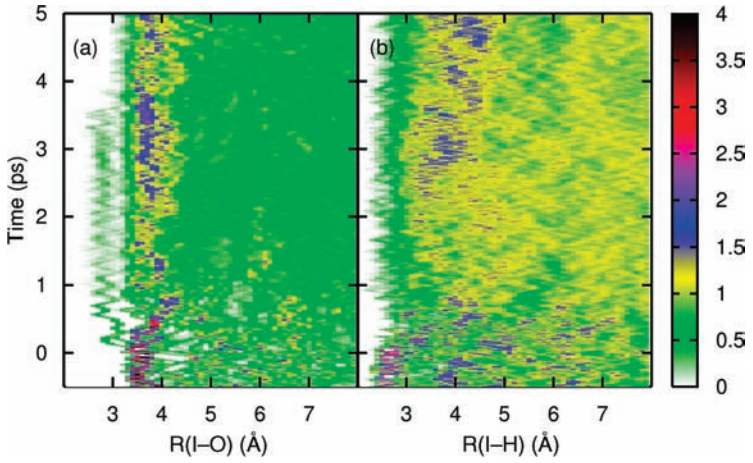

Figure 7. Time evolution of the I^0–O (**a**) and I–H (**b**) radial distributions for the first 5 ps following the removal of an electron from iodide. These distributions are obtained from an average over 15 starting configurations over the entire time range. Note the departure of both RDFs from the iodide equilibrium configuration before $t = 0$. Reprinted with the permission from Ref. [35].

In order to understand the subpicosecond transient spectra, we simulate the time evolution of the I–O and I–H radial distribution functions (RDF), shown in Fig. 7 averaged over 15 QM/MM MD simulations. Here, we observe that upon ultrafast creation of iodine there is a prompt expansion of the cage within 200 fs. However, the development of a hydrophobic solvation shell, that is, moving out and reorientation of the water molecules so that their protons point toward the solvent, is a complex process that requires 3–4 ps. After the breakup of the first shell, in which most molecules move away from the iodine, one comes closer (Fig. 7a) and forms a complex with the iodine atom, with an average probability of 0.4. The formation of this complex, which may be favored by the previously identified anisotropy of the solvent cage around iodide [182,183], results in a blue shift of the valence orbitals of iodine according to quantum chemistry calculations (Fig. 6a), leading to the broadening on the blue side of the subpicosecond transient spectra (Fig. 6b). The blue shift arises from a combination of the $I^0(5p^5)$ with the $1b_1$ orbital of water, leading to the formation of a 3-electron bond, similar to that already reported for Cl^0 [184] and Br^0 [185]. Importantly, this complex only survives the time it takes the solvent shell to build up a network of hydrogen-bonded water molecules. Only once the hydrogen bonds have reached their steady-state regime is the lone water molecule pulled toward the bulk, probably because the interaction with the water molecules of the cavity overwhelms the weak $I^0 \cdots (OH_2)$

interaction. For comparison, Fig. 6a also shows the blue shift of the 2s-2p transition upon the formation of I_2^-, which we also observed, but at much later times [35].

B. Spin-Crossover Molecular Systems

As an illustration of the performance of the high-repetition rate scheme, described in Section II.C.1, we investigated the photoinduced spin crossover in Fe^{II} molecular complexes, in which the low-spin to high-spin transition can be induced by optical excitation [186]. One of these complexes, $[Fe(bpy)_3]^{2+}$, had previously been characterized in detail using ps XAS at 1 kHz repetition rate [33,186–188]. The results obtained with the recently implemented high-repetition rate scheme (§C) are shown in Fig. 8 illustrating the 30-fold increase in S/N compared to the 1 kHz scheme [37], allowing transient changes to be measured in the preedge region of the spectrum. Similar changes were reported by Nozawa et al. [189] for another Fe(II) complex using a kHz pump–probe scheme at the Photon Factory, but the data acquisition times were significantly longer. These transitions contain information about the spin state of the molecule and are a test benchmark for theoretical simulations [190].

Already for static XAS, the increased sensitivity of the spectra is a challenge to theory. The spectrum of $[Fe(bpy)_3]^{2+}$ in the low-spin (ground) state contains a number of preedge features, which need to be properly analyzed in order to understand the nature of their changes upon photoexcitation. Figure 9 shows a comparison between the experimental spectrum and the calculated spectrum using TD-DFT. As previously noted, for such simulations the use of a localized Gaussian basis set limits them to transitions below the IP and therefore we do not attempt to describe those occurring at higher energy, which have previously been discussed in Refs [187,188]. The agreement between the simulated and experimental spectrum is satisfactory. These calculations show that the weak preedge features at low energies are transitions into states arising from the mixing of ligand orbitals with the empty iron 3d orbitals, while the higher-energy ones correspond to mixing of ligand orbitals with the iron 4p orbitals (see Fig. 9 insets, for orbitals corresponding to the A, B, and C features).

C. Solvent Effects

The molecular structure is usually extracted from an EXAFS spectrum by performing a fit (outlined in Section III.A). Here, the important scattering paths are optimized to give the best agreement with the experimental data. However, for molecules in solution additional care should be taken in accounting for the solvent, especially when the X-ray absorbing atom is directly exposed to it. In such cases, the close proximity (<6 Å) of the solvent molecules means that the X-ray absorption spectrum is likely to reflect scattering pathways that includes them.

In a recent paper, Penfold et al. [191] used QM/MM MD to demonstrate the significance of the solvent effect on the ground state XANES and EXAFS

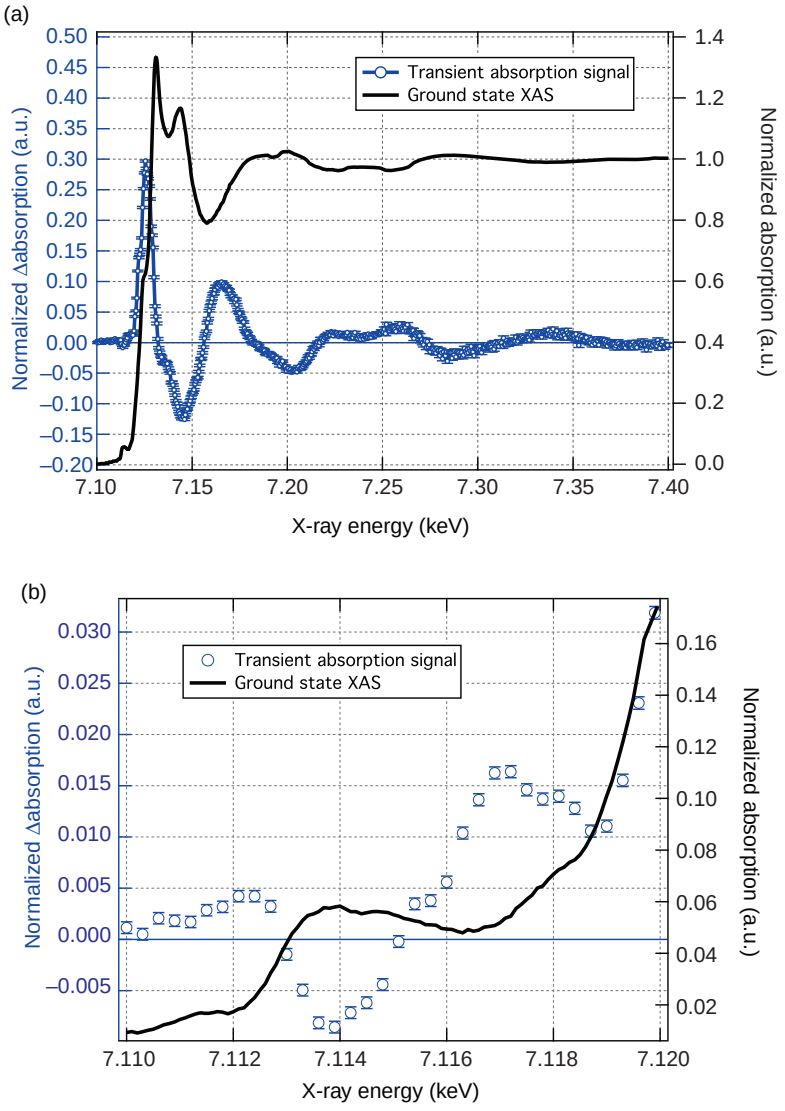

Figure 8. (**a**) Ground state XAS (black curve) and transient XAS measured 50 ps after excitation (blue markers) of aqueous $[Fe(bpy)_3]^{2+}$ using the high-repetition rate setup at the microXAS beamline at the Swiss Light Source. (**b**) Zoom of the preedge XAS spectrum showing the 1s→3d transitions and how they change upon low-spin to high-spin excitation. Reproduced from Ref. [37].

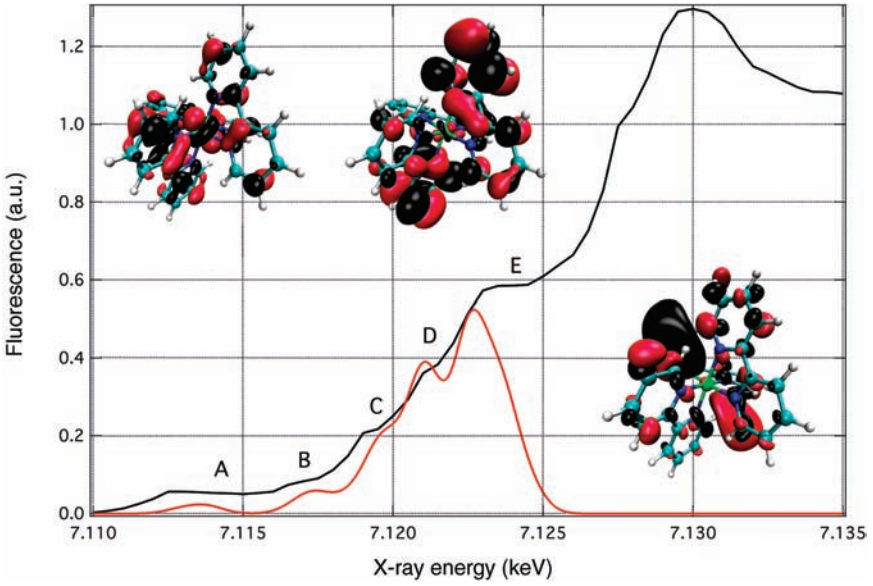

Figure 9. A zoom of the ground state (low spin) experimental (black line) and calculated (red line) near-edge spectrum of $[Fe(bpy)_3]^{2+}$ measured at the Fe K-edge. The simulations were performed using the TD-DFT method implemented within the ORCA package [164]. The simulated oscillator strengths have been broadened with a Lorentzian function to account for core hole lifetime effect. Inset are the molecular orbital plots for the excited states with the largest oscillator strengths corresponding to (from left to right) the A, B, and C features.

spectra [192–194] of the $Pt_2(P_2O_5H_2)_4]^{4-}$ (abbreviated PtPOP) complex in water, *N*,*N*-dimethylformamide, and ethanol. In Fig. 10a, we show the EXAFS spectrum from the QM/MM MD configurations for which the surrounding water molecules have been neglected. In contrast, Fig. 10b, shows the same configurations, but this time including the solvent molecules within a 6 Å radius around the Pt. One can see that this immediately results in a significant shift of the spectra. For water (red line) all of the peaks in the EXAFS spectrum shift by approximately 10 eV, in the case of DMF (green line) the shift is between 0 and 5 eV, with slight differences between the peaks, and for ethanol the shift is between 15 and 20 eV for each peak. These shifts, in the absence of the solvent, would be accounted for by further structural changes of PtPOP, and this therefore would be expected to lead to errors in the extracted structural parameters.

As discussed in Section III.D, these results highlight implications for the analysis of XAS with high time resolution (e.g., using an X-FEL) for which the solvent response to the photoexcitation will have to be explicitly taken into account. Solvent effects have clearly been observed using ultrafast optical spectroscopy of

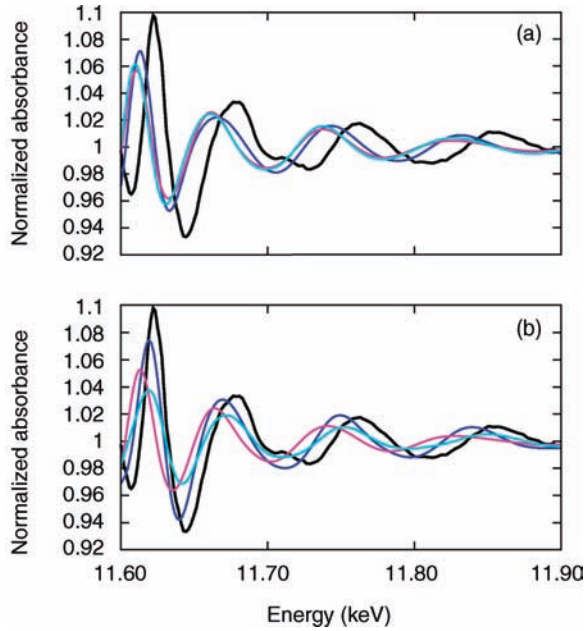

Figure 10. The experimental (black) and calculated EXAFS from the 20 configurations from the QM/MM simulations in water (dark blue), *N*,*N*-dimethylformamide (purple), and ethanol (light blue). (**a**) Considering only the Pt-POP molecule. (**b**) The Pt-POP molecule with 6 Å sphere of solvent around the platinum atoms. Figure reproduced from Ref. [191].

PtPOP, affecting both the excited state vibrational relaxation and the intersystem crossing from singlet to triplet states [195].

D. Intramolecular Charge Transfer

Understanding the structure and bonding of metal carbonyl diimine (*N*,*N*) complexes is a challenging problem, with implications to the description of the electronic structure of organometallics and in particular, the role of the metal d-orbitals and the metal–ligand π bonding. The [$ReBr(CO)_3$(bpy)] complex is a notable example and it exhibits a highly mixed and complex electronic structure [196–198]. The highest occupied molecular orbital has a mixed character between Re and Br, and therefore the electronic excitation has been predicted to have a $ReBr(CO)_3 \rightarrow$ N,N CT character, which is referred to as a metal/ligand-to-ligand charge-transfer (MLLCT) state, but this has never been directly observed. XAS is ideal in this respect as it can probe the oxidation state change at both the Re-L_3 and the Br-K edges.

Figure 11a shows the steady-state Re L_3 spectrum (black trace) of the complex. The main white line arises from transitions into the empty 5d orbitals, a common feature for the L-edge spectra of transition metal complexes. Higher energy features arise from SS and MS, among others, from scattering paths along the linear carbonyl bonds due to the so-called focusing effect [199]. Figure 11b shows

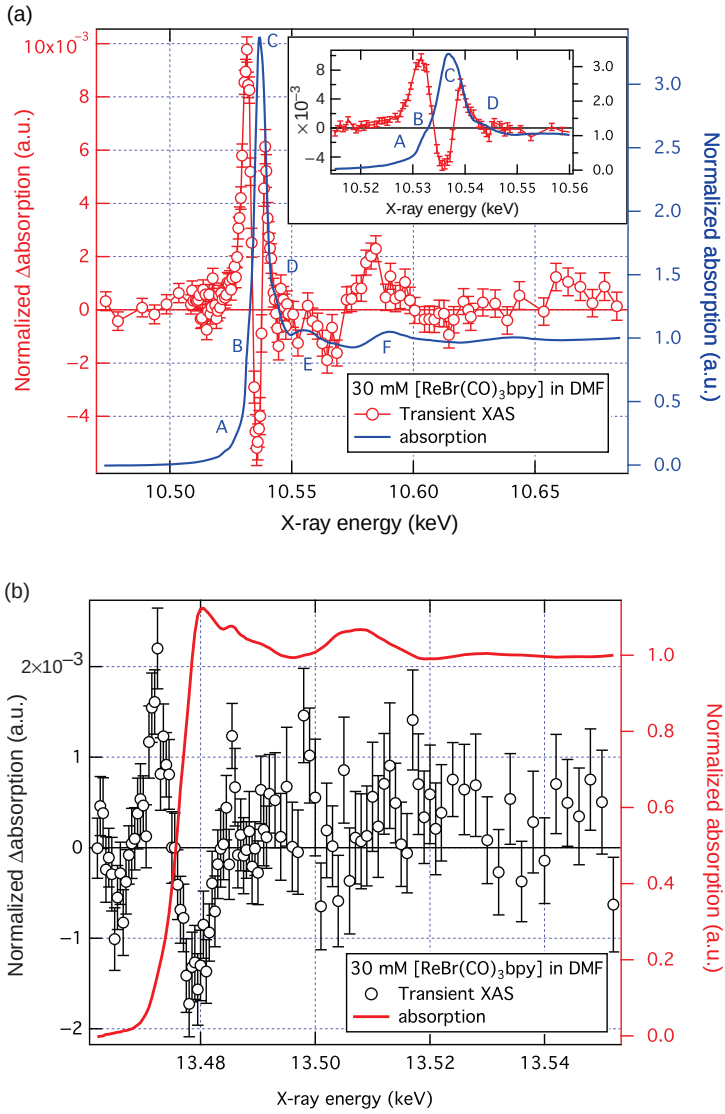

Figure 11. (**a**) Normalized ground state (blue line) and transient XAS of [ReBr(CO)$_3$(bpy)] in DMF (red markers) measured 50 ps after 355 nm excitation around the Re L_3-edge in the fluorescence yield mode. Inset: a zoom into the near-edge region to show the details of the XANES region. (**b**) The Br K-edge measured in the transmission mode. The ground state XAS is shown in red. The results of this figure have been published [200].

the steady-state Br K-edge (red trace) in which all features are due to MS. Upon excitation into the lowest CT state, the system relaxes into the triplet state faster [201] than the temporal resolution of the experiment (>50 ps). Both the Re L_3- and Br K-edge (Fig. 11b) transient spectra exhibit new preedge absorption peaks at 10.531 and 13.473 keV, which are attributed to the Re $2p_{3/2} \rightarrow 5d$ and the Br $1s \rightarrow 4p$ transitions, respectively, and arise from the creation of a hole in the Re–Br moiety by electron transfer to the bpy ligand. This establishes the MLLCT nature of the triplet excited state for the first time.

However, this type of metal complexes represents a limit to the current theoretical approaches. First, the origin of the A feature (Fig. 11a) is, due to its position, likely to derive from states that are dominated by ligand character, corresponding to the low-lying valence orbitals of CO and bpy. However, all of the above theoretical approaches failed to give a description of this feature and therefore its origin is as yet unconfirmed. In addition, the Br K-edge XANES (Fig. 11b) spectrum exhibits a significant solvent effect in acetonitrile and *N*,*N*-dimethylformamide. As in the case of PtPOP, described in Section IV.C, this could in principle be described using QM/MM MD simulations. However, the Br valence potential has a very nonspherical character and it cannot be described within the MT approximation. The current implementations of non-MT approaches are computationally too expensive, such that solvent effects cannot be quantified at present.

V. OUTLOOK

This chapter focuses on recent advances in the theory of static and time-resolved XAS of liquid solutions and on recent experimental developments in time-resolved XAS. As far as theory is concerned, the last decade has seen significant progress. MS approaches can now routinely used beyond the QPA, and in addition, efficient numerical implementation and parallelization means that such calculations are very fast [202]. The most significant remaining limitation of this approach is the MT potential, but work is underway to solve this problem. Beside MS theory, there has also been significant progress in using alternative theories. These include TD-DFT and post-HF methods extended to core-level spectroscopies and the FDMNES method. Although these methods tend to be computationally more intensive, they offer a high level of insight into the structure of near-edge spectra. Nevertheless, there is still much work to be done, especially in giving consistent quantitative agreement. This is likely to be even more important for the significant increase in spectral and temporal resolution expected with X-FELs, for which the *quasistatic* approximation will no longer hold and simulations will be required to explicitly include the excited state dynamics, nonadiabatic effects, and the surrounding environment and its response to a perturbation. Also, we have stressed the importance of including solvent effects in the simulation of spectra, as

neglecting them may, in many cases, lead to incorrect structural determination of the solute.

On the experimental side, the major development in ps XAS, which can now can be considered a routine technique for molecular systems in solution, has been the implementation of MHz repetition rates. In addition to bringing a significant increase in S/N, it also opens the possibility to perform time-resolved XAS studies on samples that can be measured with a solubility of <1 mM, such as proteins in physiological conditions [37]. These significant increases in sensitivity are unraveling finer details of the spectra, which call for a higher level of theory. Also, high-repetition rate optical pump/X-ray probe experiments open the possibility to perform photon-hungry experiments such as X-ray emission spectroscopy (XES) [5,88,203–205] and resonant inelastic X-ray scattering (RIXS) [206] of dilute systems in solution with ps time resolution. In addition, ps X-ray scattering and diffraction experiments are also possible. Beyond the limitations of third-generation synchrotrons, X-FEL's offer many exciting opportunities due to their significant increase in temporal resolution and per-pulse X-ray flux, provided problems due to time and intensity fluctuations are solved. X-FELs will undoubtedly play a significant role in the future of time-resolved XAS but it is also clear that synchrotrons will continue to contribute substantially to the field through the advent of the high-repetition rate technique. In addition, the low flux per pulse at synchrotrons will ensure less damage due to nonlinear X-ray effects than the XFEL pulses, even though the per second fluxes at these two sources are comparable. All these developments in experimental methodologies promise a detailed mapping of the valence electronic and geometric structure of the species under study and of their environment with atomic scale temporal and spatial resolution. Together with the push for theoretical improvements, the field of ultrafast X-ray spectroscopies promises to deliver new insight into the light-induced phenomena of chemical, biochemical and physical systems.

ACKNOWLEDGMENTS

We thank all of our coworkers over the years on the various ultrafast XAS studies. This work is supported by the NCCR-MUST of the Swiss National Science Foundation.

REFERENCES

1. D. C. Koningsberger and R. Prins. *X-ray Absorption: Principles, Applications, Techniques of EXAFS, SEXAFS, and XANES*, Wiley-Interscience, 1988.
2. J. Stöhr, *NEXAFS Spectroscopy*, volume 25 of *Springer Series in Surface Sciences*, Springer, 1996.
3. J. J. Rehr, *Rev. Mod. Phys.* **72**(3), 621–654 (2000).

4. P. Lee and G. Beni, *Phys. Rev. B* **15**(6), 2862–2883 (1977).
5. F. de Groot, *Chem. Rev.* **101**(6), 1779–1808 (2001).
6. P. Lee, P. Citrin, P. Eisenberger, and B. Kincaid, *Rev. Mod. Phys.* **53**(4), 769–806 (1981).
7. F. de Groot, *Coord. Chem. Rev.* **249**, 31–63 (2005).
8. C. Bressler and M. Chergui, *Chem. Rev.* **104**, 1781–1812 (2004).
9. M. Chergui and A. H. Zewail, *Chem. Phys. Chem.* **10**, 28–43 (2009).
10. S. L. Johnson and C. J. Milne, *Trac-Trends Anal. Chem.* **29**(6), 497–507 (2010).
11. L. X. Chen, *Annu. Rev. Phys. Chem.* **56**, 221–254 (2005).
12. D. M. Mills, A. Lewis, A. Harootunian, J. Huang, and B. Smith, *Science* **223**, 811–813 (1984).
13. I. Alperovich, G. Smolentsev, D. Moonshiram, J. W. Jurss, J. J. Concepcion, T. J. Meyer, A. V. Soldatov, and Y. N. Pushkar, *J. Am. Chem. Soc.* **133**, 15786–15794 (2011).
14. M. Gennari, J. Pecaut, S. DeBeer, F. Neese, M.-N. Collomb, and C. Duboc, *Angew. Chem.* **124**, 5780–5784 (2011).
15. S. DeBeer-George, T. Petrenko, and F. Neese. *J. Phys. Chem. A* **112**, 12936–12943 (2008).
16. E. F. Aziz, N. Ottosson, S. Bonhommeau, N. Bergmann, W. Eberhardt, and M. Chergui, *Phys. Rev. Lett.* **102**, 068103 (2009).
17. S. Della-Longa, A. Arcovito, M. Girasole, and J. L. Hazemann, *Phys. Rev. Lett.* **87**, 155501 (2001).
18. A. Arcovito, D. C. Lamb, G. U. Nienhaus, J. L. Hazemann, M. Benfatto, and S. Della Longa, *Biophys. J.* **88**(4), 2954–2964 (2005).
19. A. Arcovito, M. Benfatto, M. Cianci, S. S. Hasnain, K. Nienhaus, G. U. Nienhaus, C. Savino, R. W. Strange, B. Vallone, and S. D. Longa, *Proc. Nat. Acad. Sci. USA* **104**(15), 6211–6216 (2007).
20. J. Welnak, A. K. Raychaudhuri, W. Ng, and F. Cerrina, *Nucl. Instrum. Methods Phys. Res. A* **347**, 372–375 (1994).
21. E. I. Solomon, R. K. Szilagyi, S. DeBeer George, and L. Basumallick, *Chem. Rev.* **104**(2), 419–458 (2004).
22. R. H. Holm, P. Kennepohl, and E. I. Solomon, *Chem. Rev.* **96**(7), 2239–2314 (1996).
23. L. X. Chen, *J. Elec. Spectrosc. Relat. Phenom.* **119**(2), 161–174 (2001).
24. L. X. Chen, W. J. H. Jager, G. Jennings, D. J. Gosztola, A. Munkholm, and J. P. Hessler, *Science* **292**(5515), 262–264 (2001).
25. C. Bressler, M. Saes, M. Chergui, D. Grolimund, R. Abela, and P. Pattison, *J. Chem. Phys.* **116**, 2955 (2002).
26. M. Saes, F. van Mourik, W. Gawelda, M. Kaiser, M. Chergui, C. Bressler, D. Grolimund, R. Abela, T. E. Glover, P. Heimann, R. W. Schoenlein, S. L. Johnson, A. M. Lindenberg, and R. W. Falcone, *Rev. Sci. Instrum.* **75**(1), 24–30 (2004).
27. L. X. Chen, *Angew. Chem., Int. Ed. Eng.* **43**(22), 2886–2905 (2004).
28. C. Bressler, R. Abela, and M. Chergui, *Z. Kristallogr.* **223**, 308–321 (2008).
29. C. Bressler and M. Chergui, *Annu. Rev. Phys. Chem.* **61**, 263–282 (2010).
30. M. Chergui, *Acta Crystallogr. Sec. A* **66**, 229–239 (2010).
31. W. Gawelda, C. Bressler, M. Saes, M. Kaiser, A. N. Tarnovsky, D. Grolimund, S. L. Johnson, R. Abela, and M. Chergui, *Phys. Scr.* **T115**, 102–106 (2005).
32. R. W. Schoenlein, S. Chattopadhyay, H. H. W. Chong, T. E. Glover, P. Heimann, C. V. Shank, A. A. Zholents, and M. S. Zolotorev, *Science* **287**(5461), 2237–2240 (2000).

33. C. Bressler, C. J. Milne, V. T. Pham, A. ElNahhas, R. M. van der Veen, W. Gawelda, S. L. Johnson, P. Beaud, D. Grolimund, M. Kaiser, C. N. Borca, G. Ingold, R. Abela, and M. Chergui, *Science* **323**, 489–492 (2009).
34. H. Wen, N. Huse, R. W. Schoenlein, and A. M. Lindenberg, *J. Chem. Phys.* **131**(23), 234505 (2009).
35. V. T. Pham, T. J. Penfold, R. M. van der Veen, F. Lima, A. el Nahhas, S. L. Johnson, P. Beaud, R. Abela, C. Bressler, I. Tavernelli, C. J. Milne, and M. Chergui, *J. Am. Chem. Soc.* **133**, 12740–12748 (2011).
36. N. Huse, H. Cho, K. Hong, L. Jamula, F. M. F. de Groot, T. K. Kim, J. K. McCusker, and R. W. Schoenlein, *J. Phys. Chem. Lett.* **2**, 880–884 (2011).
37. F. A. Lima, C. J. Milne, D. C. V. Amarasinghe, M. H. Rittmann-Frank, R. M. van der Veen, M. Reinhard, V. T. Pham, S. Karlsson, S. L. Johnson, D. Grolimund, C. Borca, T. Huthwelker, M. Janousch, F. van Mourik, R. Abela, and M. Chergui, *Rev. Sci. Instrum.* **82**, 063111 (2011).
38. A. M. March, A. Stickrath, G. Doumy, E. P. Kanter, B. Krässig, S. H. Southworth, K. Attenkofer, C. A. Kurtz, L. X. Chen, and L. Young, *Rev. Sci. Instrum.* **82**(7), 073110 (2011).
39. L. Stebel, M. Malvestuto, V. Capogrosso, P. Sigalotti, B. Ressel, F. Bondino, E. Magnano, G. Cautero, and F. Parmigiani, *Rev. Sci. Instrum.* **82**(12), 23109 (2011).
40. W. A. Barletta, J. Bisognano, J. N. Corlett, P. Emma, Z. Huang, K. J. Kim, R. Lindberg, J. B. Murphy, G. R. Neil, D. C. Nguyen, C. Pellegrini, R. A. Rimmer, F. Sannibale, G. Stupakov, R. P. Walker, and A. A. Zholents, *Nucl. Instrum. Methods Phys. Res. A* **618**, 69–96 (2010).
41. R. Abela and B. D. Patterson, *Trends Anal. Chem.* **29**, 538–543 (2010).
42. S. Khan, *J. Mod. Opt.* **55**(21), 3469–3512 (2008).
43. S. Debeer-George, T. Petrenko, and F. Neese, *Inorg. Chim. Acta* **361**, 965–972 (2008).
44. M. Stener, G. Fronzoni, and M. de Simone, *Chem. Phys. Lett.* **373**, 115–123 (2003).
45. N. A. Besley and F. A. Asmuruf, *Phys. Chem. Chem. Phys.* **12**(38), 12024 (2010).
46. O. Bunău and Y. Joly, *J. Phys.: Condens. Matter* **21**, 345501 (2009).
47. P. Wilmott, *An Introduction to Synchrotron Radiation:Techniques and Applications*, Wiley, September 2011.
48. W. Gawelda, *Time-resolved X-ray absorption spectroscopy of transition metal complexes*, Ph.D. thesis, EPFL, 2006.
49. S. Eisebitt, T. Böske, and J. E. Rubensson, *Phys. Rev. B* **41**, 14103–14109 (1993).
50. J. Jaklevic, J. A. Kirby, M. P. Klein, and A. S. Robertson, *Solid State Commun.* **23**, 679–682 (1977).
51. Z. Tan, J. I. Budnick, and S. M. Heald. *Rev. Sci. Instrum.* **60**, 1021–1025 (1989).
52. A. Iida and K. Hirano, *Nucl. Instrum. Methods Phys. Res. B* **114**, 149–153, 1996.
53. R. Kodama, N. Ikeda, Y. Kato, Y. Katori, T. Iwai, and K. Takeshi, *Opt. Lett.* **21**(17), 1321–1323, 1996.
54. M. Newville, S. Sutton, M. Rivers, and P. Eng, *J. Synchrotron Radiat.* **6**, 353–355 (1999).
55. C. Borca, D. Grolimund, M. Willimann, B. Meyer, K. Jefimovs, J. Comamala, and C. David, *J. Phys.: Conf. Ser.* **186**, 012003 (2009).
56. S. Gorelick, J. Vila-Comamala, V. A. Guzenko, R. Barrett, M. Salome, and C. David, *J. Synchrotron Radiat.* **18**, 442–446 (2011).
57. K. Jefimovs, O. Bunk, F. Pfeiffer, D. Grolimund, J. F. van der Veen, and C. David, *Microelectron. Eng.* 1467–1470 (2007).

58. M. Abo-Bakr, J. Feikes, K. Holldack, P. Kuske, W. B. Peatman, U. Schade, G. Wustefeld, and H. W. Hubers, *Phys. Rev. Lett.* **90**(9), 094801 (2003).
59. V. Sajaev, M. Borland, Y. C. Chae, G. Decker, R. Dejus, L. Emery, K. Harkay, A. Nassiri, S. Shastri, G. Waldschmidt, B. Yang, P. A. Anfinrud, and V. Dolgashev, *Nucl. Instrum. Methods Phys. Res. A* **582**(1), 57–59 (2007).
60. A. A. Zholents, P. A. Heimann, M. S. Zolotorev, and J. Byrd, *Nucl. Instrum. Methods Phys. Res. A* **425**(1–2), 385–389 (1999).
61. S. Khan, K. Holldack, T. Kachel, R. Mitzner, and T. Quast, *Phys. Rev. Lett.* **97**(7), 074801 (2006).
62. P. Beaud, S. Johnson, A. Streun, R. Abela, D. Abramsohn, D. Grolimund, F. Krasniqi, T. Schmidt, V. Schlott, and G. Ingold, *Phys. Rev. Lett.* **99**(17), 174801 (2007).
63. A. A. Zholents and M. S. Zolotorev, *Phys. Rev. Lett.* **76**, 912–915 (1996).
64. P. Beaud, S. L. Johnson, E. Vorobeva, U. Staub, R. A. de Souza, C. J. Milne, Q. X. Jia, and G. Ingold, *Phys. Rev. Lett.* **103**(15), 155702 (2009).
65. S. L. Johnson, P. Beaud, C. J. Milne, F. S. Krasniqi, E. S. Zijlstra, M. E. Garcia, M. Kaiser, D. Grolimund, R. Abela, and G. Ingold, *Phys. Rev. Lett.* **100**(15), 155501 (2008).
66. S. L. Johnson, E. Vorobeva, P. Beaud, C. J. Milne, and G. Ingold, *Phys. Rev. Lett.* **103**(20), 205501 (2009).
67. S. L. Johnson, P. Beaud, E. Vorobeva, C. J. Milne, E. D. Murray, S. Fahy, and G. Ingold, *Phys. Rev. Lett.* **102**(17), 175503 (2009).
68. S. L. Johnson, P. Beaud, E. Vorobeva, C. J. Milne, E. D. Murray, S. Fahy, and G. Ingold, *Acta Crystallogr. Sect. A* **66** 157–167 (2010).
69. E. Moehr-Vorobeva, S. L. Johnson, P. Beaud, U. Staub, R. De Souza, C. J. Milne, G. Ingold, J. Demsar, H. Schaefer, and A. Titov, *Phys. Rev. Lett.* **107**(3), 036403 (2011).
70. M. Herzog, D. Schick, W. Leitenberger, R. Shayduk, R. M. van der Veen, C. J. Milne, S. L. Johnson, I. Vrejoiu, and M. Bargheer, *New J. Phys.* **14**(1), 013004 (2012).
71. S. Mariager, F. Pressacco, G. Ingold, A. Caviezel, E. Möhr-Vorobeva, P. Beaud, S. Johnson, C. Milne, E. Mancini, S. Moyerman, E. Fullerton, R. Feidenhans'l, C. Back, and C. Quitmann, *Phys. Rev. Lett.* **108**(8) (2012).
72. M. Harb, A. Jurgilaitis, H. Enquist, R. Nüske, C. V. Korff Schmising, J. Gaudin, S. L. Johnson, C. J. Milne, P. Beaud, E. Vorobeva, A. Caviezel, S. O. Mariager, G. Ingold, and J. Larsson, *Phys. Rev. B* **84**(4), 045435 (2011).
73. M. Herzog, W. Leitenberger, R. Shayduk, R. M. van der Veen, C. J. Milne, S. L. Johnson, I. Vrejoiu, M. Alexe, D. Hesse, and M. Bargheer, *Appl. Phys. Lett.* **96**(16), 161906 (2010).
74. J. M. Glownia, J. Cryan, J. Andreasson, A. Belkacem, N. Berrah, C. I. Blaga, C. Bostedt, J. Bozek, L. F. Dimauro, L. Fang, J. Frisch, O. Gessner, M. Gühr, J. Hajdu, M. P. Hertlein, M. Hoener, G. Huang, O. Kornilov, J. P. Marangos, A. M. March, B. K. McFarland, H. Merdji, V. S. Petrovic, C. Raman, D. Ray, D. A. Reis, M. Trigo, J. L. White, W. White, R. Wilcox, L. Young, R. N. Coffee, and P. H. Bucksbaum, *Opt. Express* **18**(17), 17620–17630 (2010).
75. C. Bostedt, H. N. Chapman, J. T. Costello, J. R. Crespo Lopez-Urrutia, S. Duesterer, S. W. Epp, J. Feldhaus, A. Foehlisch, M. Meyer, T. Moeller, R. Moshammer, M. Richter, K. Sokolowski Tinten, A. Sorokin, K. Tiedtke, J. Ullrich, and W. Wurth, *Nucl. Instrum. Methods Phys. Res. A* **601**(1–2), 108–122 (2009).
76. C. Pellegrini and J. Stöhr, *Nucl. Instrum. Methods Phys. Res. A* **500**, 33–40 (2003).
77. M. Beye, O. Krupin, G. Hays, A. H. Reid, D. Rupp, S. de Jong, S. Lee, W. S. Lee, Y. D. Chuang, R. Coffee, J. P. Cryan, J. M. Glownia, A. Foehlisch, M. R. Holmes, A. R. Fry, W. E. White,

C. Bostedt, A. O. Scherz, H. A. Durr, and W. F. Schlotter, *Appl. Phys. Lett.* **100**(12), 121108 (2012).

78. S. L. Johnson, P. A. Heimann, A. M. Lindenberg, H. O. Jeschke, M. E. Garcia, Z. Chang, R. W. Lee, J. J. Rehr, and R. W. Falcone, *Phys. Rev. Lett.* **91**, 157403 (2003).
79. S. L. Johnson, P. A. Heimann, A. G. Macphee, A. M. Lindenberg, O. R. Monteiro, Z. Chang, R. W. Lee, and R. W. Falcone, *Phys. Rev. Lett.* **94**(5), 4 (2005).
80. A. M. Lindenberg, I. Kang, S. Lee Johnson, T. Missalla, P. A. Heimann, Z. Chang, J. Larsson, P. H. Bucksbaum, H. C. Kapteyn, H. A. Padmore, R. W. Lee, J. S. Wark, and R. W. Falcone, *Phys. Rev. Lett.* **84**, 111–114 (2000).
81. B. Ahr, M. Chollet, B. Adams, E. M. Lunny, C. M. Laperle, and C. Rose-Petruck. *Phys. Chem. Chem. Phys.* **13**, 5590–5599 (2011).
82. H. T. Lemke, C. Bressler, L. X. Chen, D. M. Fritz, K. J. Gaffney, A. Galler, W. Gawelda, K. Haldrup, R. W. Hartsock, H. Ihee, K. H. Kim, J. Kim, J. H. Lee, M. M. Nielsen, A. B. Stickrath, W. Zhang, D. Zhu, and M. Cammarata, *J. Phys. Chem. A* (DOI: 10.1021/jp312559h).
83. J. J. Rehr and R. A. Albers, *Phys. Rev. B* **41**, 8139–8149 (1990).
84. K. Hatada, K. Hayakawa, M. Benfatto, and C. R. Natoli, *J. Phys.: Condens. Matter* **22**, 185501 (2010).
85. D. C. Koningsberger, B. L. Mojet, G. E. Van Dorssen, and D. E. Ramaker, *Top. Catal.* **10**(3), 143–155 (2000).
86. T. C. Weng, G. S. Waldo, and J. E. Penner-Hahn, *J. Synchrotron Radiat.* **12**, 506–510 (2005).
87. B. Ravel and M. Newville, *J. Synchrotron Radiat.* **12**, 537–541 (2005).
88. K. M. Lancaster, M. Roemelt, P. Ettenhuber, Y. Hu, M. W. Ribbe, F. Neese, U. Bergmann, and S. DeBeer, *Science* **334**, 974–977 (2011).
89. H. Funke, A. Scheinost, and M. Chukalina, *Phys. Rev. B* **71**(9), 094110 (2005).
90. M. Munoz, F. Farges, and P. Argoul, *Phys. Scr.* **T115**, 221–222 (2005).
91. B. Natarajan, M. E. Casida, L. Genovese, and T. Deutsch, Wavelets for density-functional theory and post-density-functional-theory calculations, in *Theoretical and Computational Methods in Modern Density Functional Theory, Amlan K. Roy, ed., Nova Science Publishers*, (October 2012, ISBN: 978-1-61942-779-2) pp. 313–356.
92. L. Genovese, B. Videau, M. Ospici, T. Deutsch, S. Goedecker, and J.-F. Mehaut, *C. R. Mecanique* **339**, 149–164 (2011).
93. T. J. Penfold, I. Tavernelli, C. J. Milne, M. Reinhard, A. El Nahhas, R. Abela, U. Rothlisberger, and M. Chergui, *J. Chem. Phys.* **138**, 014104 (2013).
94. M. Newville, *J. Synchrotron Radiat.* **8**(2), 322–324 (2001).
95. N. Binsted, *EXCURV98*, CCLRC Daresbury Laboratory computer program, 1998.
96. G. N. George, *EXAFSPAK*, http://www-ssrl.slac.stanford.edu/exafspak.html, 2001.
97. A. Filipponi, A. Di-Cicco, and C. R. Natoli. *Phys. Rev. B* **42**, 15122–15149 (1995).
98. E. A. Stern, *Phys. Rev. B* **48**, 9825–9827 (1993).
99. M. Benfatto, A. Congiu-Castellano, A. Daniele, and S. Della-Longa, *J. Synchrotron Radiat.* **8**, 267–269 (2001).
100. G. Smolentsev and A. Soldatov, *J. Synchrotron Radiat.* **13**, 19–29 (2006).
101. J. J. Rehr, J. Kozdon, J. Kas, H. J. Krappe, and H. H. Rossner, *J. Synchrotron Radiat.* **12**, 70–74 (2005).
102. C. R. Natoli, M. Benfatto, C. Brouder, M. F. Ruiz Lopez, and D. L. Foulis, *Phys. Rev. B* **42**, 1–25 (1990).

103. J. J. Rehr, R. A. Albers, and S. Zabinsky. *Phys. Rev. Lett.* **69**, 3397–3400 (1992).
104. A. R. Williams and J. van-W Morgan. *J. Phys. C: Solid State Phys.* **7**, 37 (1974).
105. H. Wende, P. Srivastava, R. Chauvistre, F. May, K. Baberschke, D. Arvanitis, and J. J. Rehr. *J. Phys.: Condens. Matter* **9**(31), L427 (1997).
106. Y. Joly, *Phys. Rev. B* **63**, 1–10 (2001).
107. W. H. Butler, A. Gonis, and X. G. Zhang, *Phys. Rev. B* **45**, 11527–11541 (1992).
108. J. J. Rehr and A. L. Ankudinov, *Coord. Chem. Rev.* **249**, 131–140 (2005).
109. Y. Joly, *Phys. Rev. B* **53**(19), 13029 (1996).
110. G. Smolentsev, S. E. Canton, J. V. Lockard, V. Sundstrom, and L. X. Chen, *J. Electron Spectrosc. Relat. Phenom.* **184**, 125–128 (2011).
111. G. Smolentsev, A. V. Soldatov, and L. X. Chen, *J. Phys. Chem. A* **112**, 5363–5367 (2008).
112. I. Alperovich, G. Smolentsev, D. Moonshiram, J. W. Jurss, J. J. Concepcion, T. J. Meyer, A. Soldatov, and Y. Pushkar. *J. Am. Chem. Soc.* **133**, 15786–15794 (2011).
113. W. Olszewski, K. Szymański, P. Zaleski, and D. A. Zając, *J. Phys. Chem. A* **115**, 13420–13424 (2011).
114. C. Witte, C. T. Chantler, E. C. Cosgriff, and C. Q. Tran, *Rad. Phys. and Chem.* **75**(11), 1582–1585 (2006).
115. K. Schwarz and P. Blaha, *Mol. Phys.* **108**, 21–23 (2010).
116. E. Gaudry, D. Cabaret, P. Sainctavit, C. Brouder, F. Mauri, J. Goulon, and A. Rogalev, *J. Phys.: Condens. Matter* **17**, 5467–5480 (2005).
117. X. Gonze, B. Amadon, and P. M. Anglade, *Comput. Phys. Commun.* **180**, 2582–2615 (2009).
118. M. Taillefumier, D. Cabaret, A. M. Flank, and F. Mauri, *Phys. Rev. B* **66**, 195107 (2002).
119. G. Lippert, J. Hutter, and M. Parrinello, *Theor. Chem. Acc.* **103**, 124–140 (1999).
120. *CP2K, A general program to perform molecular dynamics simulations*, 2006, http://cp2k.berlios.de.
121. M. Iannuzzi, *J. Chem. Phys.* **128**, 204506 (2008).
122. M. Iannuzzi and J. Hutter, *Phys. Chem. Chem. Phys.* **9**, 1599–1610 (2007).
123. C. Lee, W. Yang, and R. G. Parr, *Phys. Rev. B* **37**, 785–789 (1988).
124. A. D. Becke, *Phys. Rev. A* **38**, 3098–3100 (1988).
125. B. T. Thole and G. Van der Laan, *Phys. Rev. B* **38**(5), 3158 (1988).
126. F. M. F. de Groot, *Phys. B: Phys. Condens. Matter* **208**, 15–18 (1995).
127. E. Stavitski and F. de Groot, *Micron* **41**, 687–694 (2010).
128. J. J. Kas, A. P. Sorini, M. P. Prange, and L. W. Cambell, *Phys. Rev. B* 2007.
129. R. Manne and T. Aberg, *Chem. Phys. Lett.* **7**(2), 282–284 (1970).
130. B. W. Holland, R. F. Pettifer, J. B. Pendry, and J. Bordas, *J. Phys. C: Solid State Phys.* **11**(3), 633 (1978).
131. J. J. Rehr, C. H. Booth, F. Bridges, and S. I. Zabinsky, *Phys. Rev. B* **49**, 12347–12350 (1994).
132. D. E. Ramaker, B. L. Mojet, D. C. Koningsberger, and W. E. O'Grady, *J. Phys.: Condens. Matter* **10**(39), 8753 (1998).
133. M. Benfatto, S. della Longa, and P. D'Angelo, *Phys. Scr.* **T115**, 28–30 (2005).
134. L. Campbell, L. Hedin, J. J. Rehr, and W. Bardyszewski, *Phys. Rev. B* **65**, 064107 (2002).
135. J. J. Rehr, J. J. Kas, F. D. Vila, M. P. Prange, and K. Jorissen, *Phys. Chem. Chem. Phys.* **12**, 5503–5513 (2010).

136. L. Hedin and S. Lundqvist, *Solid State Phys.* **23**, 1 (1969).
137. B. I. Lundqvist, *Phys. Kondens. Mater.* **6**, 207 (1967).
138. B. I. Lundqvist, *Phys. Kondens. Mater.* **6**, 193 (1967).
139. W. Bardyszewski and L. Hedin, *Phys. Scr.* **32**, 439–450 (1985).
140. A. Zangwill and P. Soven, *Phys. Rev. A* **21**(5), 1561–1572 (1980).
141. J. J. Rehr, J. A. Soininen, and E. L. Shirley, *Phys. Scr.* **2005**, 207 (2005).
142. E. Runge and E. K. U. Gross, *Phys. Rev. Lett.* **52**(12), 997–1000 (1984).
143. M. E. Casida and M. Huix-Rotllant, *Annu. Rev. Phys. Chem.* **63**(1) (2012).
144. C. A. Ullrich, *Time-Dependent Density-Functional Theory*, Oxford Graduate Texts, 2011.
145. A. Dreuw and M. Head-Gordon, *Chem. Rev.* **105**(11), 4009–4037 (2005).
146. S. Hirata and M. Head-Gordon, *Chem. Phys. Lett.* **314**, 291–299 (1999).
147. K. Ray, S. Debeer-George, E. I. Solomon, K. Wieghardt, and F. Neese, *Chemistry* **13**, 2783–2797 (2007).
148. A. Dreuw, J. L. Weisman, and M. Head-Gordon, *J. Chem. Phys.* **119**(6), 2943–2946 (2003).
149. M. Roemelt, M. A. Beckwith, C. Duboc, M. N. Collomb, F. Neese, and S. DeBeer, *Inorg. Chem.* **51**(1), 680–687 (2012).
150. T. Saue, *Chemphyschem* **12**(17), 3077–3094 (2011).
151. J. Autschbach and T. Ziegler, *J. Chem. Phys.* **113**, 9410–9418 (2000).
152. J. Autschbach and T. Ziegler, *J. Chem. Phys.* **113**, 936–947 (2000).
153. G. Fronzoni, M. Stener, P. Decleva, F. Wang, T. Ziegler, E. van Lenthe, and E. J. Baerends. *Chem. Phys. Lett.* **416**, 56–63 (2005).
154. F. Wang, T. Ziegler, E. van Lenthe, S. van Gisbergen, and E. J. Baerends, *J. Chem. Phys.* **122**(20), 204103 (2005).
155. F. Wang and T. Ziegler, *J. Chem. Phys.* **123**(19), 194102 (2005).
156. A. L. Ankudinov, Y. Takimoto, and J. J. Rehr, *Phys. Rev. B* **71**, 165110 (2005).
157. S. Sharma, J. Dewhurst, A. Sanna, and E. Gross, *Phys. Rev. Lett.* **107**(18), 186401 (2011).
158. L. Reining, V. Olevano, A. Rubio, and G. Onida, *Phys. Rev. Lett.* **88**(6), 066404 (2002).
159. M. Nooijen and R. J. Bartlett, *J. Chem. Phys.* **102**, 6735 (1995).
160. S. Coriani, O. Christiansen, T. Fransson, and P. Norman, *Phys. Rev. A* **85**(2), 022507 (2012).
161. F. A. Asmuruf and N. A. Besley, *Chem. Phys. Lett.* **463**(1–3), 267–271 (2008).
162. M. Head-Gordon, R. J. Rico, M. Oumi, and T. J. Lee, *Chem. Phys. Lett.* **219**(1–2), 21–29 (1994).
163. E. F. Aziz, M. H. Rittmann-Frank, K. M. Lange, S. Bonhommeau, and M. Chergui, *Nat. Chem.* **2**, 853–857 (2010).
164. F. Neese, U. Becker, D. Ganyushin, S. Kossmann, A. Hansen, D. Liakos, T. Petrenko, C. Riplinger, and F. Wennmohs, *Max Planck Institute for Bioinorganic Chemistry*, 2012, ORCA—An *ab initio*, density functional and semiempirical program package.
165. F. Neese, *Wiley Interdiscip. Rev.: Comput. Mol. Sci.* **2**(1), 73–78 (2012).
166. F. Neese, *Inorg. Chim. Acta* **337**(0), 181–192 (2002).
167. J. P. Perdew, Density-Functional Approximation for the Correlation-Energy of the Inhomogeneous Electron-Gas. *Phys. Rev. B* **33**, 8822–8824 (1986).
168. F. Neese, T. Petrenko, D. Ganyushin, and G. Olbrich, *Coord. Chem. Rev.* **251**(3–4), 288–327 (2007).

169. A. Laio, J. VandeVondele, and U. Rothlisberger, *J. Phys. Chem. B* **106**, 7300–7307 (2002).
170. A. Laio, J. VandeVondele, and U. Rothlisberger, *J. Chem. Phys.* **116**(16), 6941–6947 (2002).
171. U. F. Röhrig, I. Frank, J. Hutter, A. Laio, J. VandeVondele, and U. Rothlisberger, Qm/mm car parrinello molecular dynamics study of the solvent effects on the ground state and on the first excited singlet state of acetone in water. *Chem. Phys. Chem.* **14**, 1177–1182 (2003).
172. U. Rothlisberger and P. Carloni, *Lect. Notes Phys.* **704**, 437–466 (2006).
173. B. F. E. Curchod, P. Campomanes, A. Laktionov, M. Neri, T. J. Penfold, S. Vanni, I. Tavernelli, and U. Rothlisberger, *Chimia* **65**(5), 330–333 (2011).
174. E. Brunk, N. Ashari, P. Athri, P. Campomanes, B. F. E. Curchod, P. Diamantis, M. Doemer, J. Garrec, A. Laktionov, M. Micciarelli, M. Neri, G. Palermo, T. J. Penfold, S. Vanni, I. Tavernelli, and U. Rothlisberger, *Chimia* **65**, 667–671 (2011).
175. E. Tapavicza, I. Tavernelli, and U. Rothlisberger, *Phys. Rev. Lett.* **98**, 023001 (2007).
176. J. C. Tully, *J. Chem. Phys.* **93**, 1061–1071 (1990).
177. I. Tavernelli, B. F. E. Curchod, A. Laktionov, and U. Rothlisberger, *J. Chem. Phys.* **133**, 194104 (2010).
178. I. Tavernelli, B. F. E. Curchod, and U. Rothlisberger, *J. Chem. Phys.* **131**, 196101 (2009).
179. L. R. Pratt and A. Pohorille, *Chem. Rev.* **102**(8), 2671–2692 (2002).
180. K. A. Dill, T. M. Truskett, V. Vlachy, and B. Hribar-Lee, *Annu. Rev. Biophys. Biomol. Struct.* **34**(1), 173–199 (2005).
181. V. T. Pham, W. Gawelda, Y. Zaushitsyn, M. Kaiser, D. Grolimund, S. L. Johnson, R. Abela, C. Bressler, and M. Chergui, *J. Am. Chem. Soc.* **129**, 1530 (2007).
182. V. T. Pham, I. Tavernelli, C. J. Milne, R. M. van der Veen, P. D'Angelo, C. Bressler, and M. Chergui, *Chem. Phys.* **371**(1–3), 24–29 (2010).
183. C. J. Wick and S. S. Xantheas, *J. Phys. Chem. B* **113**, 4141–4146 (2009).
184. M. D. Sevilla, S. Summerfield, I. Eliezer, J. Rak, and M. C. R. Symons, *J. Phys. Chem. A* **101**(15), 2910–2915 (1997).
185. C. G. Elles, I. A. Shkrob, R. A. Crowell, D. A. Arms, and E. C. Landahl, *J. Chem. Phys.* **128**, 061102 (2008).
186. A. Cannizzo, C. J. Milne, C. Consani, W. Gawelda, C. h. Bressler, F. van Mourik, and M. Chergui, *Coord. Chem. Rev.* **254**, 2677–2686 (2010).
187. W. Gawelda, V. T. Pham, M. Benfatto, Y. Zaushitsyn, M. Kaiser, D. Grolimund, S. L. Johnson, R. Abela, A. Hauser, C. Bressler, and M. Chergui, *Phys. Rev. Lett.* **98**, 057401 (2007).
188. W. Gawelda, V. T. Pham, R. M. van der Veen, D. Grolimund, R. Abela, M. Chergui, and C. Bressler, *J. Chem. Phys.* **130**(12), 124520 (2009).
189. S. Nozawa, T. Sato, M. Chollet, K. Ichiyanagi, A. Tomita, H. Fujii, S. Adachi, and S. Koshihara, *J. Am. Chem. Soc.* **132**(1), 61–63 (2010).
190. B. E. Van Kuiken and M. Khalil, *J. Phys. Chem. A* **115**(39), 10749–10761 (2011).
191. T. J. Penfold, B. F. E. Curchod, I. Tavernelli, R. Abela, U. Rothlisberger, and M. Chergui, *Phys. Chem. Chem. Phys.* **14**, 9444–9450 (2012).
192. R. M. van der Veen, C. J. Milne, V. T. Pham, A. El Nahhas, J. A. Weinstein, J. Best, C. N. Borca, C. Bressler, and M. Chergui, *Chimia* **62**, 287–290 (2008).
193. R. M. van der Veen, J. J. Kas, C. J. Milne, V. T. Pham, A. El Nahhas, F. A. Lima, D. A. Vithanage, J. J. Rehr, R. Abela, and M. Chergui, *Phys. Chem. Chem. Phys.* **12**(21), 5551–5561 (2010).
194. R. M. van der Veen, C. J. Milne, A. El Nahhas, F. A. Lima, V. T. Pham, J. Best, J. A. Weinstein, C. N. Borca, R. Abela, C. Bressler, and M. Chergui, *Angew. Chem.* **48**, 2711–2714 (2009).

195. R. M. van der Veen, A. Cannizzo, F. van Mourik, A. Vlček Jr, and M. Chergui, *J. Am. Chem. Soc.* **133**(2), 305–315 (2011).

196. A. Cannizzo, A. M. Blanco-Rodr´iguez, A. El Nahhas, J. Šebera, S. Zalis, A. Vlček Jr, and M. Chergui, *J. Am. Chem. Soc.* **130**(28), 8967 (2008).

197. A. Vlček, *Top. Organometal. Chem.* **29**, 115–158 (2010).

198. R. Baková, M. Chergui, C. D. A Vlček, and S. Zális, *Coord. Chem. Rev.* **255**, 975–989 (2011).

199. S. I. Zabinsky, J. J. Rehr, A. Ankudinov, and R. C. Albers, *Phys. Rev. B* **52**, 2995 (1995).

200. A. El Nahhas, R. M. van der Veen, T.J. Penfold, V. T. Pham, F.A. Lima, R. Abela, S. Zális, A. Vlcek, I. Tavernelli, U. Rothlisberger, C. J. Milne, and M. Chergui, *J. Phys. Chem. A* **117**, 361–369 (2013).

201. A. Cannizzo, A. M. Blanco-Rodriguez, A. El Nahhas, J. Sebera, A. Vlček, S. Zális, and M. Chergui, *J. Am. Chem. Soc.* **130**:8967, 2008.

202. J. J. Rehr and A. L. Ankudinov, *J. Synchrotron Radiat.* **10**, 43–45 (2003).

203. N. Lee, T. Petrenko, U. Bergmann, F. Neese, and S. DeBeer, *J. Am. Chem. Soc.* **132**, 9715–9727 (2010).

204. G. Smolentsev, A. V. Soldatov, J. Messinger, K. Merz, T. Weyhermuller, U. Bergmann, Y. Pushkar, J. Yano, V. K. Yachandra, and P. Glatzel, *J. Am. Chem. Soc.* **131**, 13161–13167 (2009).

205. G. Vanko, P. Glatzel, V.-T. Pham, R. Abela, D. Grolimund, C. N. Borca, S. L. Johnson, C. J. Milne, and C. Bressler, *Angew. Chem., Int. Ed.* **49**(34), 5910–5912 (2010).

206. P. Glatzel and U. Bergmann, *Coord. Chem. Rev.* **249**, 65–95 (2005).